PORE-WATER AND PROTON TRANSPORT IN POLYMER ELECTROLYTE MEMBRANE FUEL CELL: MOLECULAR DYNAMICS AND MONO- AND BIMODAL WETTING TREATMENTS OF MESOPORE HYDRATED NAFION

by

Gi Suk Hwang

A dissertation submitted in partial fulfillment
of the requirements for the degree of
Doctor of Philosophy
(Mechanical Engineering)
in the University of Michigan
2010

Doctoral Committee:

Professor Massoud Kaviany, Chair
Professor Levi T. Thompson Jr.
Associate Professor Christian M. Lastoskie
Associate Professor Adam J. Matzger

Acknowledgements

Above all, I thank God for allowing me to have wonderful and unforgettable moments in the University of Michigan, where I met and collaborated with so many outstanding people. Without their help and inputs, it would have been impossible to complete all of the work. So, I am indebted to excellent and generous professors, colleagues, and friends.

I special thank to professor Massoud Kaviany, my advisor for constant source of support and motivation with thoughtful comments and research enthusiasm. He also encouraged me to raise fundamental questions, and provided me with a lot of insights and advice on the area of academic as well as life in general. I am thankful to professors Levi Thompson, Christian Lastoskie, and Adam Matzger, my committee members, for the thesis evaluation processes and valuable comments. I express gratitude to professors Moo Hwan Kim at Pohang University of Science and Technology, and Sang Young Son at University of Cincinnati for useful discussions on Nafion pore-water. I thank to professors Michael Falk at the Johns Hopkins University, and Reinhard Hentschke at the University of Wuppertal in Germany for willingness to help me understand molecular simulations. I am also grateful to Dr. Adam Weber for con-

siderate advice on the development of the bimodal model, and to Drs. Jeffrey Gostick, Alexander Hexemer, Brian Kienitz, and Cheng Wang at Lawrence Berkeley National Laboratory for assisting with the SAXS measurements. I thank to professor Michael Hickner at the Penn State University for many communications on pore-water measurements, and to professor William R. Rossen at the University of Texas at Austin for helpful discussions on the role of snap-off in the Schröder paradox. I owe Hosop Shin, a graduate student at the University of Michigan, the temperature-dependent adsorption modeling work for Nafion, and Amélie Saint-Germain, an undergraduate international intern from Toulouse, IMFT affiliate, the development of the capillary-pressure model. I am thankful to John Mansfield at EMAL for assisting with the observation of Nafion pore-water, and to Cynthia Quann-White and Kelly Chantelois for administrative issues. I am thankful to all the former and current lab-mates, Xiulin Ruan, Baoling Huang, Jedo Kim, Dahye Min, Seungha Shin, and Hyungchul Kim for making these years enjoyable life. Finally, I appreciate my parents, parents in law, and my wife, Eun Sil Kim for supporting me through never-ending dedication and love.

This work has been supported by the sponsorship of Global Partnership Program from Ministry of Science and Technology, South Korea. This work has been partially supported by the Assistant Secretary for Energy Efficiency and Renewable Energy, Office of Fuel Cell Technologies, of the U.S. Department of Energy under contract number DE-AC02-05CH11231.

Table of Contents

List of Figures

List of Tables

List of Appendices

Nomenclature

a	constant
$a_{\mathrm{H_2O}}$	water activity
c	concentration
d	diameter
f	distribution function
Δh_{lg}	isosteric heat of adsorption
j_e	electrical current density
k	thermal conductivity
k_{B}	Boltzmann constant
l	distance, length
m	mass
n	number density
p	pressure
p	capillary pressure
q	charge
r	radius

s	liquid saturation
s_{ad}	onset of adsorbed-layer saturation
s_{im}	immobile saturation
t	time
$\boldsymbol{u}$	velocity
v	molar volume
z_e	effective atomic charge
D	diffusion coefficient
E	energy
F	Faraday constant
H	height
J_e	electric current
K	permeability
K_r	relative permeability
Kn	Knudsen number
M	atomic weight
N	number of particles
Q	heat flow
R_c	cut-off radius
T	temperature
V	volume
$\langle\ \rangle$	mean value

Greek symbols

α_{eo}	electro-osmotic coefficient
β	constant
$\Delta\varphi_e$	electrical potential
δ	adsorbed-water layer thickness
ϵ	porosity
ε	deviation
γ	van der Waals potential coefficient
λ	water content, mean free path
μ	chemical potential
ρ	density
ρ_e	electrical resistivity
τ	relaxation time
φ	potential energy, voltage
σ	surface tension
θ	contact angle

Subscripts

a	atomic
c	capillary, cell, cut-off
e	electron

eff	effective
eo	electro-osmotic coefficient
f	fine, fluid
C	coulomb
D	Debye
i	summation index, particle label
j	summation index, particle label
l	liquid
lg	liquid-gas
max	maximum
r	reduced
rl	relative
v	vapor
A	anode
C	cathode
H_2O	water
H^+	proton
O_2	oxygen

Superscripts

*	dimensionless

Abbreviations

BET	Brunauer-Emmett-Teller
CL	catalyst layer
FC	fuel cell
GDL	gas diffusion layer
G-K	Green-Kubo
MC	Monte Carlo
MD	molecular dynamics
MPL	micro porous layer
PEM	polymer electrolyte membrane

Chapter 1

Introduction

1.1 Water Management and Hydrated Nafion

Water management is a critical issue in an operation of a polymer electrolyte membrane fuel cell (PEMFC) [74, 3, 24]. The fuel cell consists of a few permeable layers, i.e., polymer electrolyte membrane (PEM), catalyst layers (CLs), micro porous layers (MPLs), and gas diffusion layers (GDLs) [74, 3]. Without sufficient water in the PEM and CLs, the proton transport and electrochemical reactions are significantly hindered, causing poor performance. In contrast, excessive water in the CLs, MPLs, and GDLs impedes reactant transport, resulting in poor performance. Thus, optimal hydration throughout the layers is essential to improving cell performance.

The optimal hydrated PEM should provide good proton conductivity [22, 106, 36, 45, 101, 1, 68, 69, 59, 19], continuous liquid water pressure with the adjacent layers [96, 48], and chemical/mechanical robustness [69]. Nafion® meets these requirements, and is considered here. Hydration of Nafion and its transport properties are related

to hydration-induced nanophase morphology, separating into hydrophobic polymer backbone and water-filled domains surrounded by hydrophilic sulfonic side chains [69] as shown in Figure 1.1. The domains represent hydrated pores, and a mean domain or pore size is $\langle d_p \rangle = 4$ nm [20]. These small domains result in significant water-surface interactions compared to water-water interactions, especially in smaller domains where force fields overlap. This promotes water filling (capillary condensation) [82], and hinders transport. So, this domain-size-dependent confinement is essential to the atomic-level understanding of the hydrated-Nafion pore-water states and water/proton transport.

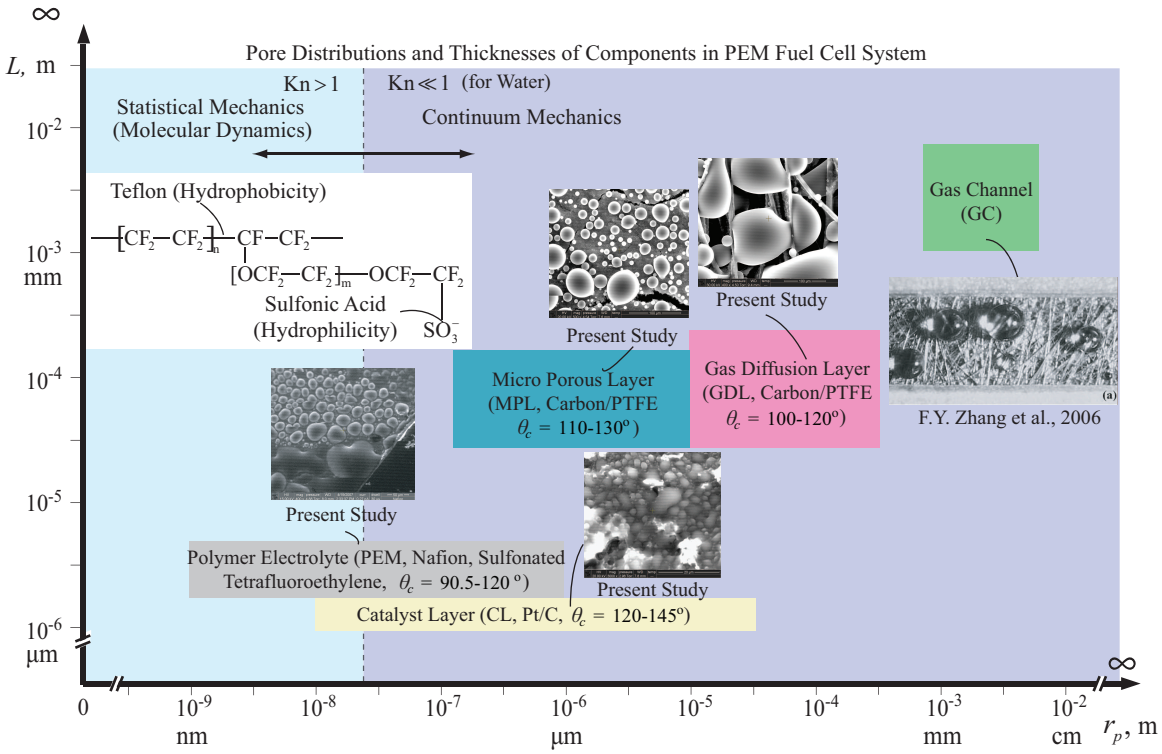

Figure 1.1: Summary of pore (domain) size distributions and layer thicknesses of the PEMFC components. Chemical composites of Nafion, contact angles of surface water, and ESEM images are also shown.

Many attempts have been made to explore the hydrated Nafion. Its hydration-

induced polymer structural changes and resulting water wetting have been addressed from the polymer-dynamics perspectives, using molecular [59, 87] and macromolecular approaches [36, 45, 51, 50, 13, 42, 83, 97, 66, 35]. Macroscopically, its water uptake [104, 44, 7, 39, 75, 72] and the resulting proton conductivity [101, 26, 10, 11, 98, 14] have been also examined. These have contributed to defining the roles of the backbone and pore geometries in the water states and proton transport. However, these studies have not yet addressed the important roles of the pore-size distribution (and the presence of a pore network) in the Nafion adsorption and transport. Here, we propose a pore-level bimodal wetting model with the hydrated Nafion treated as a rigid network of pores (no swelling), i.e., hydration independent, and propose a thermally-induced hydrophobicity to explain decrease in adsorption with increase in temperature.

While the criticality of hydration Nafion is explored in this study, importance of hydration in CL, MPL, and GDL is referred to the previous studies [52, 53, 78, 32].

1.2 Nafion Mesopore Confinement and Proposed Bimodal Model

An idealized bimodal pore-size distribution is proposed for hydrated Nafion, guided by our SAXS measurement, the existing pore-size distribution measurement [20], and the available bimodal pore network model [36, 45]. The large pores are represented by the mean pore size, 4 nm, while the small ones are determined by the Debye screening

length (the distance over which charge carriers screen out the surface electric field), i.e., 1 nm, and these are rendered in Figure 1.2. The dominant source of the water-surface interactions is the electrostatic force between the ionized sulfonic acid sites and the water molecules. In our molecular simulations, nanogaps are used for the pores (following section). The effective screening length can be approximated by the Debye length given as [80],

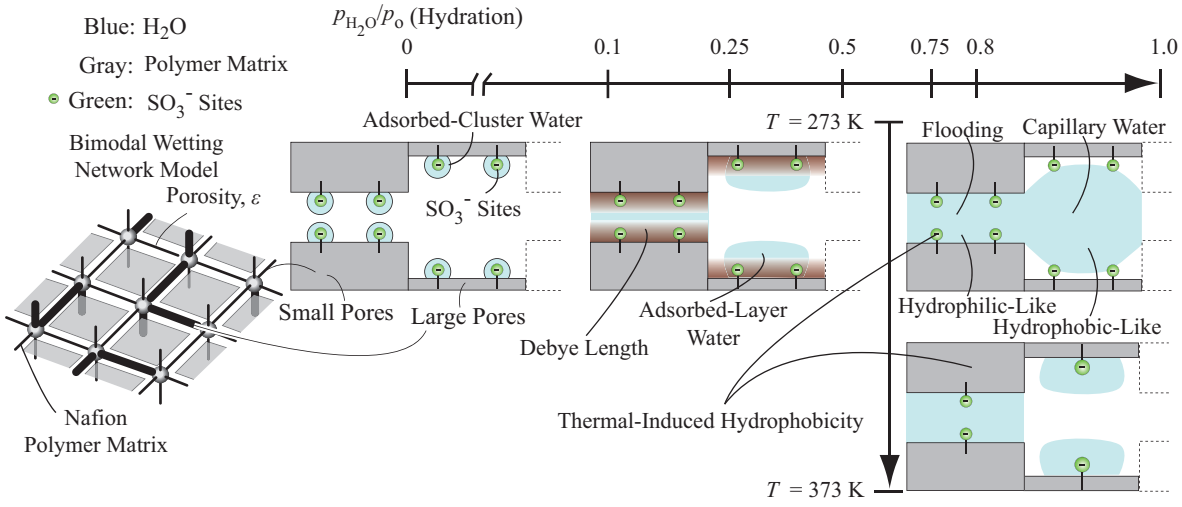

Figure 1.2: The proposed bimodal pore-size and water-wetting network model, showing hydration water morphological evolution (increasing vapor pressure at constant temperature) and thermally-induced hydrophobicity (increasing temperature at constant vapor pressure).

$$\delta_{\mathrm{D}} = \left(\frac{\epsilon_{\mathrm{o}}\epsilon_{\mathrm{r}}k_{\mathrm{B}}T}{4\pi e^2 \sum_i n_i z_{e,i}^2}\right)^{1/2}, \tag{1.1}$$

where ϵ_{o} and ϵ_r are the free-space electric and relative permittivities, k_{B} is the Boltzmann constant, T is the temperature, n_i and $z_{e,i}$ are the number density and the number of conduction electrons per contributing ions. $\delta_{\mathrm{D}} = 0.23$ nm is predicted using an equivalent weight (EW) 1100 g/mole, a density 2 g/cm^3 [95], and two types

of ions, the sulfonic acid and hydronium. This is nearly one layer of the adsorbed water, using a hard sphere diameter $d_{H_2O} = 0.3$ nm [14]. This effective interaction length is consistent with the predictions using the Pekar-Marcus relation [25] and the mean field Poisson-Boltzmann theory [23]. Using 1.5 adsorbed-water layer and the two confining pore surfaces, a 1 nm nanogap (pore size) is set as the small pore size.

The proposed bimodal pore size is critically related to the bimodal water wetting. Although the measured surface contact angle is overall hydrophobic [103, 95, 38], the small pores (1 nm) allow for overlapping surface forces and behave as hydrophilic-like. In contrast, the large pores (4 nm) do not allow for such overlapping, and behave as hydrophobic-like. Also, this bimodal wetting description is consistent with the contrasting contact angles of the sessile water droplet on Nafion surface, i.e., hydrophobic advancing and hydrophilic receding contact angles [103, 38].

In the presence of a pore network, this model requires thermodynamic equilibria among neighboring pores and porous layers (at the boundaries), as well as the overall porosity [20]. As they are in contact with a vapor reservoir, the gaseous and adsorbed phases are physically connected with those in the adjacent pores, and must be equilibrated with a prescribed chemical potential. The smaller pores readily form capillary condensate, i.e., full liquid saturation, due to the pore confinement, compared to the larger pores [82]. In contact with a liquid reservoir, the hydrated pores have capillary pressure, i.e., van Genuchten model [48, 54], and must equilibrate with that in the reservoir or those in the neighboring porous layers, i.e., catalyst layers (CLs) and gas diffusion layers (GDLs) [52, 78, 96, 53, 43, 72, 48]. Using a homogeneous-hydrophobic water-wetting treatment, the capillary pressure in the smaller pores becomes very high

(due to very small meniscus radius) and is in turn readily emptied. This contradicts the above descriptions for the vapor equilibrated reservoir, and is not physical. The proposed small (hydrophilic) and large (hydrophobic) bimodal model fulfills the thermodynamic requirements, allowing for a consistent treatment of the vapor and liquid equilibria. This model is further justified using SAXS analysis and molecular simulation below. In addition, hydrated Nafion has a porosity of 0.4 [20, 93], and using the lateral pore size $L_X = L_Z = 6$ nm guided by our experimental result at RH = 100% (Table 2.1), the pore population ratios are 0.53 and 0.47 and the pore volume ratios are 0.22 and 0.78, for $L_{Z,p} = 1$ and 4 nm, respectively.

1.3 Statement of Objective and Scope of Thesis

The primary objective of this study is to develop atomic-level models to elucidate the mesopore-confined water state and water/proton transport. A comprehensive, unified, multiscale approach is developed for this investigation, which combines the pore network and molecular dynamics (MD). The following chapters are divided based on the proposed pore-network models and the resulting pore-water state and water/proton transport.

Chapter 2 develops monomodal and bimodal wetting network models to represent the Nafion characteristics, i.e., mesopores with heterogeneous wetting, and to explain pore-water state and water/proton transport which will be discussed in the following chapters. In the monomodal, the four pore-water morphologies [48], i.e., the adsorbed cluster, adsorbed layer, capillary, and flooding waters are discussed. In

the bimodal wetting treatment [47], bimodal pore-size confinement and the resulting bimodal water-wetting are discussed. Then, the bimodal network will be used to predict the water adsorption and the capillary transition, the water self diffusion, the proton conductivity, and the liquid saturation distribution. This proposed network is validated by SAXS measurements and prediction and by the isosteric heat of adsorption found from MD.

Chapter 3 predicts the water adsorption and capillary transition using the grand canonical molecular dynamics - Monte Carlo simulation (GCMD-MC) with prescribed uniform sulfonic acid density. Adsorption is also predicted by the modified Brunauer-Emmett-Teller (BET) adsorption theory and its morphological transition to capillary state is also predicted using the Saam-Cole theory [48, 82] and the Kelvin-Cohan relation [12, 14]. The temperature-dependent adsorption is also discussed, and the thermally-induced hydrophobicity is proposed for the observed delay in the capillary transition at high temperatures.

Chapter 4 investigates water self-diffusion using MD and the Green-Kubo autocorrelation relation [30, 55]. We discuss the hindered diffusion mechanism and the bulk-like diffusivity at large water contents. The role of pore-size distribution on the diffusion is also addressed.

Chapter 5 continues discussion of the proton conductivity predicted using molecular dynamics simulation, while considering both the diffusive and the hopping (rotational diffusion) proton conductivities. The observed proton conductivity increase (jump) is related to the onset of bulk-like diffusive and hopping conductivity by capillary transition, and this becomes less pronounced at elevated temperatures due to

the delayed capillary transition.

Chapter 6 examines the capillary liquid water flow through PEM, which is related to the liquid saturation distribution. The monomodal and bimodal water-wetting network models both reasonably predict the liquid saturation, with a continuous liquid saturation distribution throughout all the layers.

Chapter 7 summarizes the highlights of this work and proposes future directions for the related research.

Chapter 2

Mono- and Bi-modal Water-Wetting Models

2.1 Introduction

A pore network model is crucial for bridging the gap between the atomic-level water behavior and the proton transport and macroscopic measurements or models. However, as will be reviewed in the following section, the existing pore network models have overlooked the pore-size related water-wetting states, and their effects on water/proton transport. Here, we propose mono- and bimodal pore-size/water-wetting model to explore atomic-level water state and water/proton transport (aided by molecular simulation) as a unified treatment.

2.2 Existing Pore Network Models

There have been many attempts to model the Nafion morphologies such as the bimodal cluster network model [36, 45], structural inversion model [34], sandwich-like model [42], percolation channel model [94], parallel channels model [83], as shown in Figures 2.1(a)-(e). The bimodal, cluster network model [Figure 2.1(a)], with 1 and 4 nm pore sizes, is based on thermodynamic equilibrium and network percolation calculations. Although this model has been popular, no direct evidence has been provided, and a recent study has concluded that this network could not support the SAXS measurement [83]. In the structural inversion model (b), the swelling and dissolution processes have been phenomenologically described, but no quantitative study has been done yet. In the sandwich-like model (c), a simple nanogap has been proposed, but the water states and the resulting water/proton transports have not been addressed. In the percolation model (d), the Schröder paradox has been highlighted between water content, $\langle \lambda_{H_2O} \rangle = 14$ and 22, and attempted to relate it to the capillary percolation. However, the capillary percolation occurs at lower hydration $\langle \lambda_{H_2O} \rangle = 5$ or 6, due to the strong surface interactions [48]. In the long parallel channel model (e), the long channels give large water diffusion and enhanced proton conductivity even at low hydration, by best fitting the SAXS results in the range of the scattering wave vector $0.05 < q < 0.4$ nm^{-1}. However, it has not addressed water morphology related to transport properties in the presence of a pore network. In summary, these existing Nafion models have not addressed criticalities of the pore-size distribution related wetting behaviors and their consequences in pore-

water states and water/proton transport including their temperature dependency.

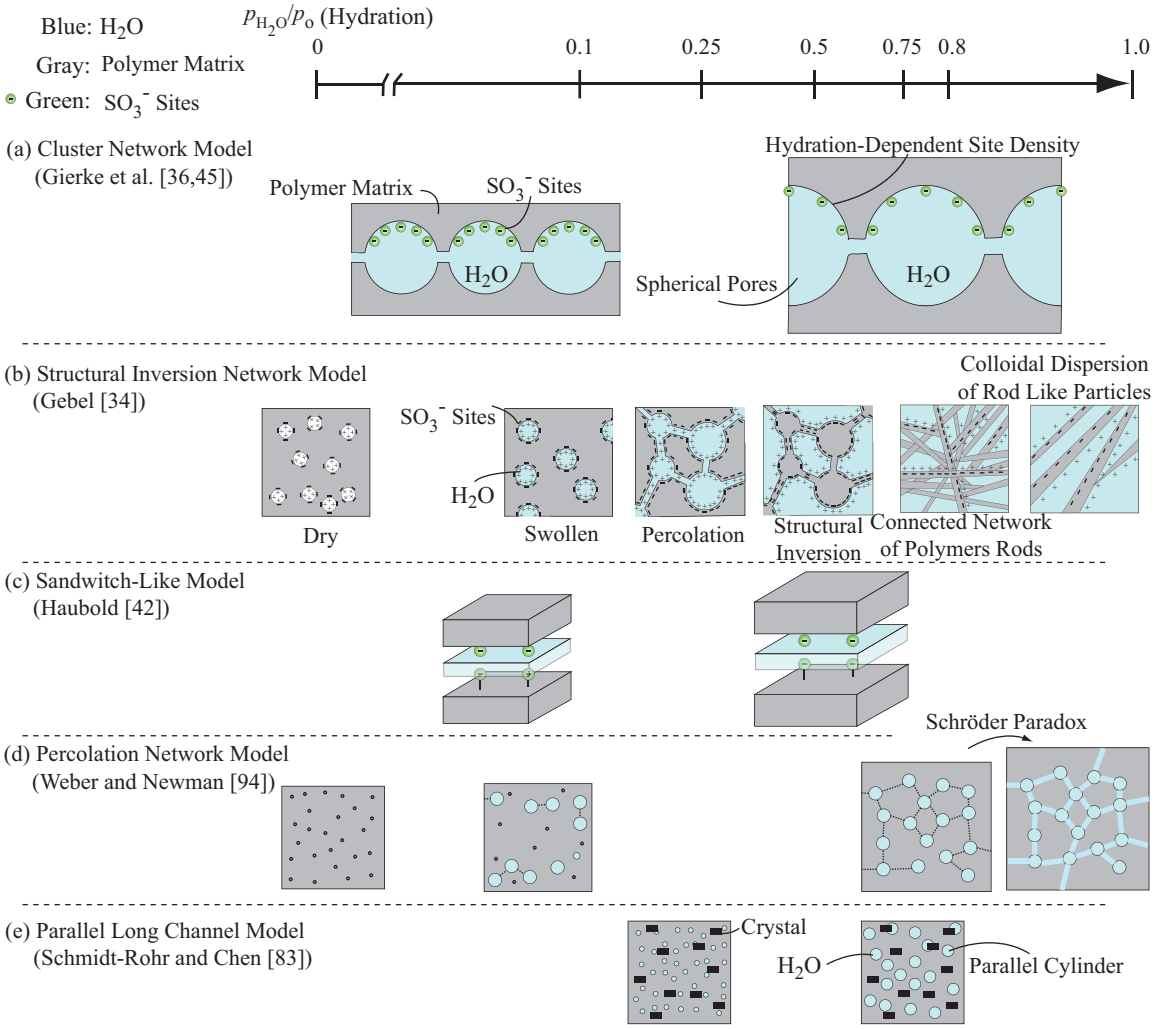

Figure 2.1: (a) The cluster network model [36, 45]. (b) The structural inversion network model [34]. (c) The sandwich-like model [42]. (d) The percolation network model [94]. (e) The parallel, long channels network model [83].

2.3 Monomodal Model

2.3.1 Pore-Water Morphologies

We use the monomodal wetting model, i.e., a mean pore size and a heterogeneous water-wetting treatment. We also use the four liquid pore-water morphologies in Nafion, i.e., the adsorbed-cluster, adsorbed-layer, capillary, and flooded. These are postulated based on the available experimental results [45, 94, 99, 101] and our observations using environmental scanning electron microscopy (ESEM, FEI Quanta 200 3D). The images are taken at 3 to 6°C and 4.02 to 4.88 torr. These environmental temperature and pressure are much different from those in operating PEMFC. In addition, the surface water behavior is not the same as the pore water due to complex pore morphology and overlapping surface forces. However, we assume the wetting is not significantly different under similar humidity and temperature. So we cautiously use the ESEM observed surface water, as shown in Figures 2.2 and 2.3, as a guide for the pore-water behavior.

Figure 2.2(a) shows pore structure, including heterogeneous pore sizes (pore throat, pore body) and surface wettability. Some of water molecules are ionized by dissociated proton from hydrogen molecule, and mainly forms hydronium H_3O^+. These hydroniums are adsorbed by hydrophilic side chains, whereas neutral waters (H_2O) are attracted by the van der Waals forces (physisorption-motivated percolation). The locally wetted water is designated as adsorbed-cluster water. Since this remains mechanically and electrically isolated, it is immobile and provides no proton conductivity. This isolated adsorbed water is readily observed in ESEM image which

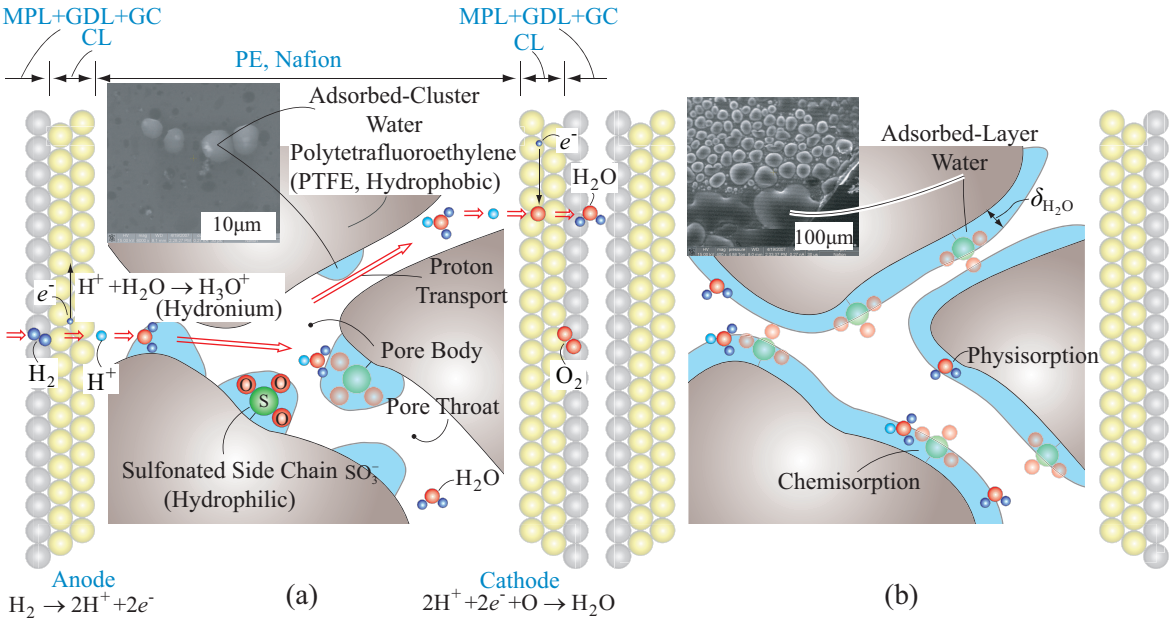

Figure 2.2: Evolution of pore-water morphologies (states) within hydrated Nafion pores including ESEM images of microsize surface water. (a) Isolated adsorbed-cluster water on hydrophilic sites, showing a hydrophilic-like contact angle. Nafion pore-size heterogeneity (small throat, and large body) and surface wetting heterogeneity (hydrophobic Nafion backbone, and hydrophilic sulfonic acid SO_3^-). Hydrogen dissociates on the anode side, and oxygen, proton, and electron reacts on the cathode side. Ionized water (hydronium) is adsorbed by the hydrophilic side chain. (b) The adsorbed-cluster water grows and coalesces with the adjacent water bodies to form the adsorbed-layer water. Adsorbed-layer water thickness is designated as δ_{H_2O}.

shows hydrophilic-like contact angle and localized wetting by sulfonated side chains. In Figure 2.2(b), the isolated, adsorbed-cluster water grows and coalesces with the adjacent waters, which is named as the adsorbed-layer water. These waters create the adsorbed-layer percolation channels, resulting in an onset of the proton conductivity. However, it still barely moves due to strong interactions with Nafion surface. This adsorbed-layer water is also observed in the ESEM image. In Figure 2.3(a), further growth leads to instability due to increase in the adsorbed-water energy (chemical potential [82]). This adsorbed layer screens the surface force and mitigate the surface-

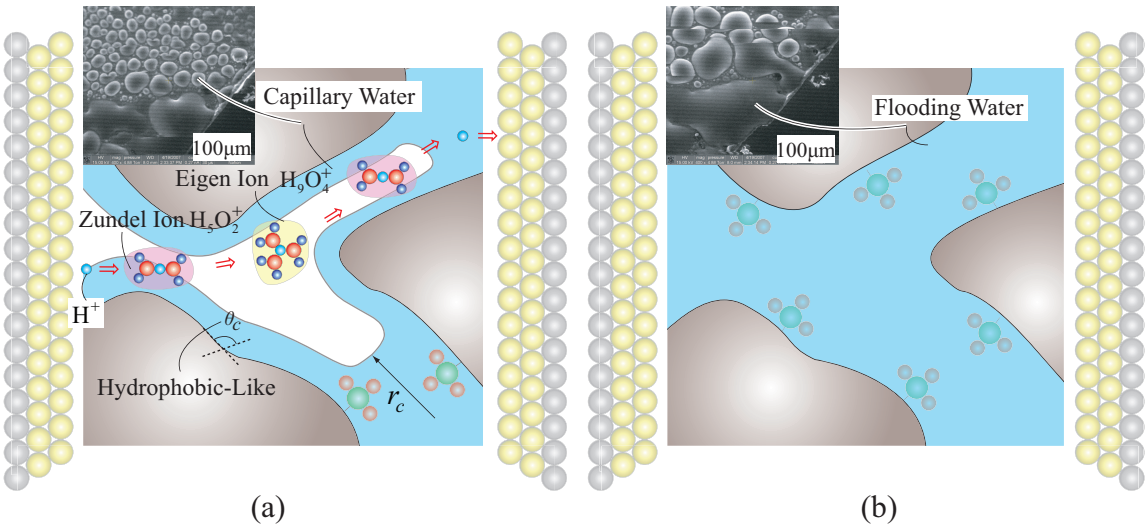

Figure 2.3: Continued from Figure 2.2. (a) In small pore space (pore throat), capillary transition occurs due to overlapping strong surface forces, and forms percolation channels for proton transport by hopping via Zundel and Eigen cations [1, 106, 22, 91, 67, 68]. The meniscus radius in the capillary pressure r_c is also shown. (b) Flooded pore. The water transport and proton conductivity are maximized.

force heterogeneity, showing hydrophobic-like wetting [70]. This is readily seen from an apparently hydrophobic-like contact angle in the ESEM image. Then, at the threshold, morphological transition to capillary state occurs. This capillary water forms capillary-percolation channels by connecting adjacent capillary water bodies. These channels provide for large proton pathways through a bulk-like liquid water (hopping over Zundel and Eigen cations) [1, 106, 22, 91, 67, 68]. The meniscus curvature radius r_c will be predicted using the morphological transition theory. There are still large empty spaces in this state. Mesopores significantly confine the fluid, leading to a rarefied gas (large Knudsen number) [57, 55], while their strong surface force alters the chemical potential of the fluid (near surfaces) and results in adsorption and capillary transition [82, 64]. The confinement effects are most pronounced for $\sigma_{LJ}/r_p > 0.25$ (where σ_{LJ} is the Lennard-Jones separation constant and r_p is the

pore size) [100, 64, 84]. Although $\sigma_{LJ}/r_p \sim 0.15$ for the water-Nafion, the confinement effects are still expected. Water morphological transitions are also observed in our preliminary molecular dynamics (MD) simulation for water confined in homogeneous nanogaps [46] (The original study was for Ar-Pt, however we simulate water-Nafion using a single site, nonpolarized water intermolecular potential [90]). In some simulations, we find direct transition from adsorbed-cluster (i.e., not covering the entire surface) to capillary water. This scattered-adsorbed or capillary water leads to an indefinite meniscus and contact angle in the Laplace-Young (L-Y) and Kelvin equations, and a vague gas pressure (due to only a small number of gas molecules in the pore). The Nafion structure also changes by swelling. However, L-Y and Kelvin equations had been used in mesopores [82] and in Nafion [96, 14, 20, 10]. Moreover, the percolative penetration model [14] using the available standard porosimetry results [20] predicts the Nafion sorption isotherm [85]. Due to current lack of an alternative water transport model, we also use the capillary pressure, relative permeability, and bulk liquid viscosity for pore water transport in Nafion, while we are guided by the results form MD simulation [46], infrared spectroscopy [62], and proton conductivity measurements [68, 19]. In Figure 2.3(b), the empty pores are flooded by capillary imbibitions (Section 3.3) and the proton conductivity is maximized. This flooding is also found in the ESEM micrographs.

The morphological transitions among these states are adsorbed-cluster to adsorbed-layer, adsorbed-layer to capillary, and capillary to flooding water. The adsorbed-cluster to adsorbed-layer water, i.e., adsorbed-layer percolation channel is related to the onset of the proton conductivity [36, 14, 101]. It is designated as $\lambda_{\mathrm{H_2O},ad}$ or $s_{ad,\mathrm{PE}}$.

Assuming homogeneous pore radius $r_p = 1$ nm and pore length $L_p = 20$ nm, equivalent weight, EW = 1100 g/mole, density, $\rho_{\mathrm{PE}} = 2$ g/cm^3 (dry) [95], the porosity $\epsilon_{\mathrm{PE}} = 0.4$ [93], liquid sulfonic acid density $\rho_{\mathrm{SO}_3^-} = 1.831$ g/cm^3 [16], it is predicted that each side of a cubic equivalent sulfonic acid $\delta_{\mathrm{SO}_3^-} = 4.464$ Å and the average space $L_s = 4.22$ Å between the adjacent sulfonic sites [shown in Figure 3.1]. Then, the first transition is predicted at $\lambda_{\mathrm{H_2O},ad} = 2.5$, using further assumptions of 1.5 hard sphere water molecules ($d_{\mathrm{H_2O}} = 2.77$ Å [14]) in the lateral spacing and one water molecule adsorbed on the top of sulfonic acid [Figure 3.1]. This prediction shows a good agreement with the empirical result $\lambda_{\mathrm{H_2O},ad}$ = 2-2.3 in [36, 14, 101]. Similarly, $s_{ad,\mathrm{PE}} = 0.18$ is obtained using Eq. (C.2) and $\epsilon_{\mathrm{PE}} = 0.4$ [93]. The adsorbed-layer to capillary and capillary to flooding transitions will be discussed in Section 3.3.

2.3.2 Pore-Size Distribution in Nafion and Its Role in Liquid Saturation

Pore-size distribution is important to the capillary percolation-channel size (occupying pore). The occupying pore volume using the standard porosimetry method with water, is measured [20], and the results are represented as the liquid saturation and water content using Eqs. (C.1) and (C.2) in Appendix A, as shown in Figure 2.4. The measured pore radii vary from 1 to 1000 nm ($r_p > 1000$ nm is ignored since those may due to Nafion rough surface pores), and mean pore radius $\langle r_p \rangle = 2$ nm is estimated using Eq. (D.1) in Appendix B. In addition, the empirically determined morphology transition radius using the vapor-equilibrated and liquid-equilibrated isotherms [4]

shows good agreements with the measurement [20]. The three morphological transitions, $\lambda_{\mathrm{H_2O},ad} = 2.3$, $\lambda_{\mathrm{H_2O},im} = 5$, and $\lambda_{\mathrm{H_2O},c\text{-}f}$ are also indicated to determine the percolation-channel size (radius). Here, the percolation-channel sizes are empir-

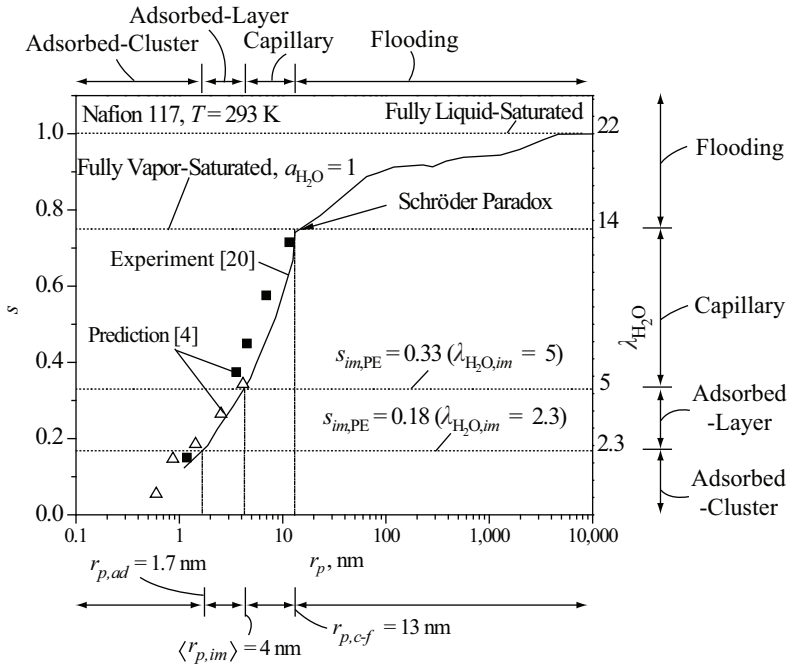

Figure 2.4: Variation of liquid saturation (or water content) with respect to the pore radius r_p from water sorption of Nafion [20, 4]. Fully liquid-saturated and vapor-saturated states ($a_{\mathrm{H_2O}} = 1$, or $\lambda_{\mathrm{H_2O}} = 14$) are shown. The adsorbed-layer saturation $s_{ad,\mathrm{PE}}$, immobile saturation $s_{im,\mathrm{PE}}$, mean pore size radius $\langle r_p \rangle$, and the transition in the Schröder paradox are also shown.

ically determined as $1.7 < r_p < 4$ for the adsorbed-percolation, $4 < r_p < 13$ for the capillary-percolation channel, and $r_p > 13$ for the Shröder paradox. Note that the predictions for the first and second transitions are made based on $r_p = 1$ nm and $\langle r_p \rangle = 2$ nm, respectively, while the corresponding, occupied pore radii are $r_{p,ad} = 1.7$ nm, and $\langle r_{p,im} \rangle = 4$ nm, which are larger than those assumed in the analyses. These discrepancies may be related to the oversimplifying of the complex topology of pores in Nafion. The homogeneous pore assumption may represent only the effective

pore throat [percolation channels, Figure 2.3(a)], ignoring variable area pores (pore bodies). So, we expect the actual $r_{p,ad}$ and $r_{p,im}$ to be larger than 1 nm and $\langle r_p \rangle = 2$ nm. It is found that the capillary-percolation channels form by selectively occupying pores, and this in turn results in low liquid saturation distribution as observed the previous study [43].

2.4 Bimodal Model

In contrast to the monomodal model, we use an idealized bimodal pore-size distribution for hydrated Nafion, guided by our SAXS measurement, the existing pore-size distribution measurement [20], and the available bimodal pore network model [36, 45]. The large pores are represented by the mean pore size, 4 nm, while the small ones are determined by the Debye screening length (the distance over which charge carriers screen out the surface electric field), i.e., 1 nm, and these are rendered in Figure 1.2. The detailed discussions are given in Section 1.2.

In our model, the dominant source of water-surface interaction is the electrostatic force between the hydrophilic, ionized sulfonic side chain and the water molecules. There are also intermolecular interactions between the hydrophobic polymer backbone and water molecules, but they are weaker. So, our simplified interactions with the polymer matrix do not significantly influence the water-wetting and transport properties, as shown the later sections.

Although chemical changes in hydrated Nafion have not been addressed yet [69], a chemical change occurs near the domain surface during hydration/dehydration [49].

Water equilibrates with RSO_3^- and RSO_3H the hydrophilic side chains, resulting in $RSO_3^- + H_3O^+ \rightarrow RSO_3H + H_2O$. So, we add the same number of H_3O^+ to the molecular simulation in the nanogap to neutralize SO_3^- sites (details in Appendix A).

For temperature dependence, we note that Nafion is viscoelastic [65] with flexible chains[76, 77], and its morphology evolves with temperature. Here we use the same pore network and decrease the sulfonic acid site density, as shown in Figure 1.2 (further discussion in later sections).

2.4.1 Small Angle X-ray Scattering (SAXS)

The bimodal model is validated by SAXS measurements and analyses. Nafion 117 specimens were tested using SAXS at the Advanced Light Source of Lawrence Berkeley National Laboratory, with X-ray wavelength 1.239 Å. For the test, the samples are boiled for one hour in a 1M H_2SO_4 solution to remove any ionic impurities and to ensure a fully protonated state. Samples were mounted in a sealed sample holder such that they hung above a pool of pure water (or saturated KCl solution) and allowed to equilibrate for 48 hours. The sample holder is shown in Figure 2.5. The sample was hung from the lid while water, a salt solution or desiccant was placed in the bottom of the reservoir. The holes through the holder allowed unimpeded X-ray access to the hanging sample. The holes were covered with a Kapton film to create a sealed environment. Immediately prior to obtaining the SAXS spectra, the fully humidified Nafion specimen to be tested was transfer to a new sample holder filled with desiccant. SAXS spectra were collected every 5 minutes over 4 hours as the

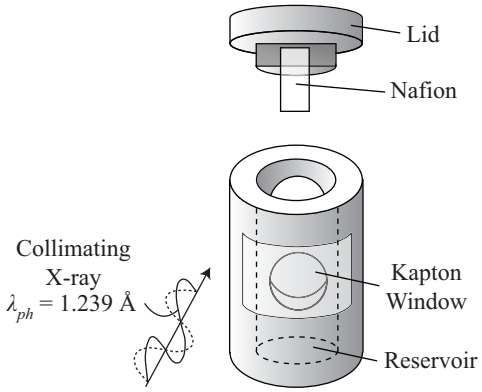

Figure 2.5: The Nafion holder for SAXS measurement.

sample dried. Similarly, the samples equilibrated with KCl (85% RH) were moved into a sample holder with LiCl (11% RH) and allowed to equilibrate for 4 hours, while collecting SAXS spectra. The background attenuation is dependent on the humidity of the air. A background was collected for each test and assumed to apply for the duration of the drying (i.e. constant relative humidity equal to either 0% for desiccant or 11% for LiCl). The measured scattering X-ray intensities are subtracted from the background scattering, and then are normalized by the transmitted intensity and the results are shown in Figure 2.6. The peaks at $q \sim 0.15$ and 0.185 Å^{-1} characterize hydrated Nafion morphologies and are related to characteristic length of the hydrated domains, which is 3.3 to 4.2 nm. These peaks shift lower q with an increase in RH due to the swelling and domain growth.

To predict the measured SAXS, a three-layer (polymer matrix, adsorbed-water including sulfonic acid sites, and gaseous water layers), parallel-piped with random pore orientations, pore network is constructed as shown in Figures 2.7(a) and (b). This is similar to the sandwich-like model [42], by treating the adsorbed water as

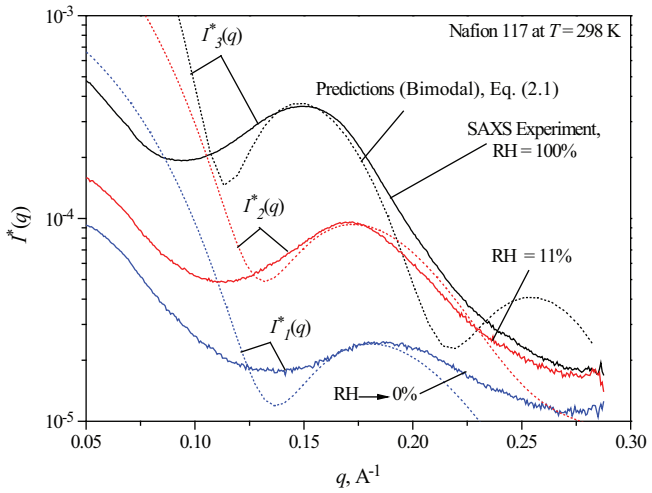

Figure 2.6: The measured, normalized SAXS intensity I^*(q) as a function of the scattering wave vector q for Nafion 117 at RH = 0, 11, and 100%, at $T = 298$ K, and $p = 1$ atm. Variations of the predicted intensity Eq. (2.2) are also shown.

layers and adding polymer matrix layers. Thus, the original model is modified as

$$I^*(q) = \alpha \int_0^1 \frac{2}{\pi} \int_0^{\pi/2} S^2(L_{X,u}, \phi, a) \mathrm{d}\phi [\Delta n_{e,p}(S(L_{Z,u}, a) - S(L_{Z,p}, a)) + \Delta n_{e,ad,H_2O}(S(L_{Z,p}, a) - S(L_{Z,g}, a)) + \Delta n_{e,g,H_2O} S(L_{Z,g}, a)]^2 \mathrm{d}a, \quad (2.1)$$

where

$$S^2(L_{X,u}, \phi, a) = \frac{\sin[0.5qL_{X,u}\cos(\phi)(1-a^2)^{1/2}]}{0.5qL_{X,u}\cos(\phi)(1-a^2)^{1/2}} \frac{\sin[0.5qL_{X,u}\sin(\phi)(1-a^2)^{1/2}]}{0.5qL_{X,u}\sin(\phi)(1-a^2)^{1/2}} L_{X,u}^2, \quad (2.2)$$

$$S(L_{Z,u}, \phi, a) = \frac{\sin(0.5qL_{Z,u}a)}{0.5qL_{Z,u}a} L_{Z,u}, \quad a = \cos(\phi). \quad (2.3)$$

where S is the form factor, Δn_e is the electron density variation, and α is the scaling factor. Using the proposed bimodal pore-size, the predicted $L_{Z,g}$ (next chapter), and the pore population ratio, the predicted results for RH = 0, 11, and 100% show

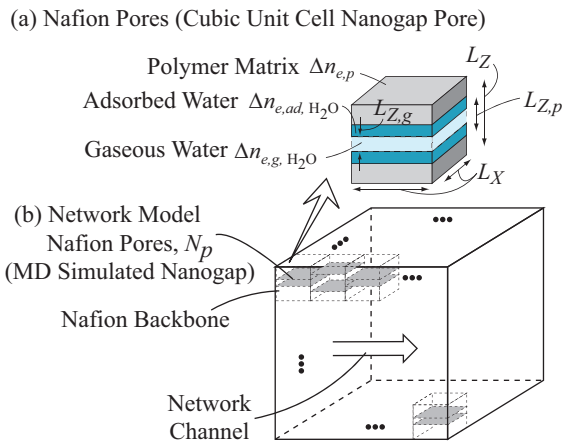

Figure 2.7: (a) The proposed, hydrated, 3-layer nanogap structure. (b) The bimodal pore-size and water-wetting network.

reasonable agreement with the measured data, particularly near $q > 0.125$ Å as shown in Figure 2.6. The peak in q (characteristic length) is related to an average distance associated with the L_X or L_Z, $L_{Z,p}$ and $L_{Z,g}$ [Figure 2.7(a)], and the domain-size distribution. The predictions using the bimodal pore-size model with the parameters given in Table 2.1, agree with the measured peak at $q \sim 0.15$ to 0.185 Å^{-1}. However, there are discrepancies in the slopes around the peaks, and at RH = 100% there is another peak at high q. This is caused by the simplified pore-size distribution (bimodal pore size), while giving reasonable intensities over $q = 0.005$ to 0.4 Å in the state-of-art SAXS analysis [83].

2.4.2 Isosteric Heat of Adsorption

Our molecular simulation results further validate the bimodal wetting model. The simulation procedures are given in Appendix A. In general, the isosteric heat of adsorption at the small adsorption provides the strength of the adsorbate/adsorbent

Table 2.1: Summary of the SAXS model parameters for Eq. (2.2).

Parameters	Magnitude		
RH %	0	11	100
L_Z, nm	4.8	5.0	6.0
$L_{Z,g}$, nm in $L_{Z,p} = 1$ nm	1	0	0
$L_{Z,g}$, nm in $L_{Z,p} = 4$ nm	4	3.7	0
$\Delta n_{e,p}$, Å^{-3}	-0.0875	-0.0875	-0.18
$\Delta n_{e,ad}$, Å^{-3}	0.02	0.02	0.08
$\Delta n_{e,g}$, Å^{-3}	-0.0045	-0.0045	-0.1

interactions [79]. Using A.1, the heat of adsorption is calculated as a function of the number of adsorbed-water layer $N_{ad,\mathrm{H_2O}}$ for the bimodal pore size, as shown in 2.8. The total adsorbed-water layer thickness (summation of two layers from top and bottom) using $d_{\mathrm{H_2O}} = 0.3$ nm is also shown at the top x axis. The Debye screening length is also marked. As the adsorbed-water layer grows beyond the Debye length, the heat of adsorption decreases towards the bulk value, i.e., the heat of evaporation (46 kJ/mol at $T = 300$ K for MSPC/E water model [15]), since the surface interactions are significantly screened. In the small pores, the heat of adsorption is nearly doubled for small adsorption, and still remains slightly higher compared to the bulk heat of evaporation at large adsorption. In contrast, in the large pore it is only 15% higher for the small adsorption and then becomes nearly the same as the bulk. This indicates that the small pores critically confine water, i.e., behaving hydrophilic-like, whereas the large pores behave hydrophobic-like, due to no significant confinement.

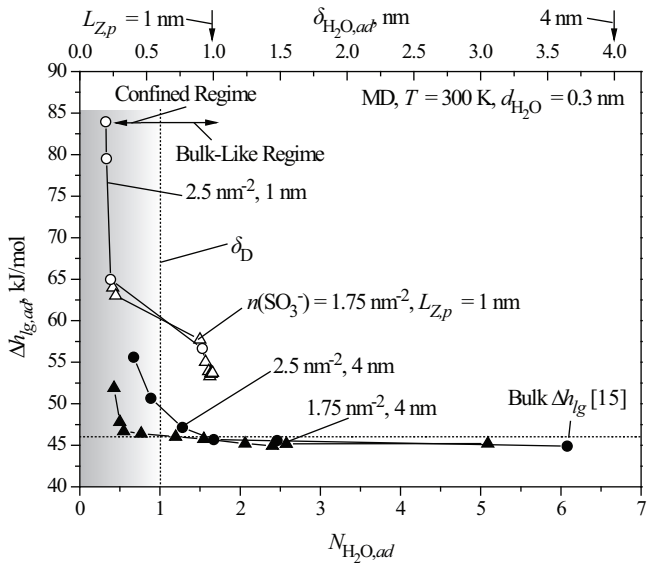

Figure 2.8: Variations of the MD predicted isosteric heat of adsorption $\Delta h_{lg,ad}$ as a function of the number of adsorbed water layers, and the total adsorbed-water thickness for the two pore sizes and for the sulfonic acid densities. The bulk heat of evaporations for MSPC/E water at $T = 300$ K is also shown [15], along with the Debye screening length.

2.5 Swelling and Mechanical Constraint of Nafion

Nafion swells with hydration, influencing its water uptake [29, 98, 61] and transport properties [101]. We use the pores, which are equivalent to the swollen membrane, and hydration/temperature independent. Although this predicts the experimental results, it overestimates the water uptake and transport at low hydration. However, recent experiments shows that the mechanical compression does not significantly change the water uptake [86]. The mechanical constraint by the adjacent layers in fuel cell changes the water uptake and transport properties, since physical binding appears to rearrange the hydrophilic sites. At elevated temperatures, Nafion softens and the swelling-induced wetting and transport changes become more pronounced.

2.6 Summary

This chapter poses and describes the pore-water morphologies and the criticalities of their transitions in the monomodal model, and points to the coexistance of the small, hydrophilic-like pores and the large, hydrophobic-like pores in the network in the bimodal model. The monomodal model is developed based on ESEM observation, and the bimodal model is based on the Debye length, which is further validated by SAXS measurements/analyses and MD results for the isosteric heat of adsorption. These models provide comprehensive insights into the atomic-level pore-water states and transport models and allow for the prediction of the adsorption (Chapter 3), water-self diffusivity (Chapter 4), and proton conductivity (Chapter 5), and capillary flow (Chapter 6). Although a rigid polymer matrix is considered here, physical and chemical changes in polymer matrix with hydration (swelling), and its anticipated swelling effects are also discussed.

Chapter 3

Pore-Water States:Adsorption and Capillary Condensation

3.1 Importance of Capillary Condensation on Water/Proton Transport

The adsorbed-layer to capillary water is important to the proton conductivity jump and the hydraulic pore-water transport. The proton conductivity jump is found at $\lambda_{H_2O} \sim 5$ in Nafion 117 [101] and other ionomeric membranes [104], and is related to the capillary transition [101, 18]. This postulation is further supported by the onset of dilution of ^{1}H intradiffusion at $\lambda_{H_2O} > 6$ in [102], an absorbed bonding energy shift from hydronium to liquid water at $\lambda_{H_2O} = 5$ to 6 using Fourier transform infrared transmission spectroscopy [62]. For the hydrodynamic pore-water transport, the electro-osmotic flow towards the cathode results in narrow capillary percolation

channels (adsorbed-layer water, dryout) on the anode side of Nafion. As a result, the capillary pressure gradient is created, and then the pore-water returns towards the anode side. When the pore-water is dryout, this circulation is broken as a result of the low proton conductivity (below the jump) and the immobile pore-water (generally, adsorbed water does not move). So, this transition is set to the immobile water content $\lambda_{\mathrm{H_2O},im}$ or equivalently, the immobile saturation $s_{im,\mathrm{PE}}$ as the minimum wetting state for the hydrodynamic (capillary) pore-water transport, while the maximum wetting state is related to Schröder paradox.

3.2 Adsorption Theory: Modified BET

The BET (Brunauer, Emmett, and Teller) theory explains the multilayer physical adsorption on a homogeneous surface[21]. However, in general, it is valid only at moderate reduced pressures $p/p_{\mathrm{o}} < 0.3$, due to the simplifying assumption that the heat of liquefaction of the second and subsequent layers are equal. This theory is modified by adjusting for the excess heat of liquefaction for the second and subsequent layers at high pressures, and has successfully been used for adsorption of the hydrated Nafion assuming homogeneous wetting pore surface [14]. This modified BET model is given as [21]

$$\frac{n_{\mathrm{H_2O},ad}}{n_{\mathrm{H_2O},ad,m}} = \frac{Ck(p/p_{\mathrm{o}})}{(1-kp/p_{\mathrm{o}})[1+(C-1)k(p/p_{\mathrm{o}})]} \tag{3.1}$$

where $n_{\mathrm{H_2O},ad}$ is the number density of the adsorbed water, $n_{\mathrm{H_2O},ad,m}$ is the number density of the adsorbed water for monolayer, $C = C_{\mathrm{o}} \exp(\Delta h/k_{\mathrm{B}}T)$, $\Delta h_{ad,ex}$ is the excess of the heat of liquefaction that the second and subsequent layers leases, $k =$

$\exp(\Delta h_{ad,ex}/k_{\mathrm{B}}T)$, and p_{o} is the saturation pressure at given temperature.

3.3 Capillary Transition Theories

3.3.1 Saam and Cole Theory

The adsorbed-layer and capillary transition threshold is predicted using the Saam-Cole morphological transition theory [82]. This is related to the onset of capillary liquid flow and the proton conductivity jump which is represented by $\lambda_{\mathrm{H_2O},im}$. This transition is related to the system energy shift (chemical potential) by minimizing surface energy of adsorbed pore water. Assuming a cylindrical pore of radius r_p, as shown in Figure 3.1, the chemical potential of Nafion-water μ is given as

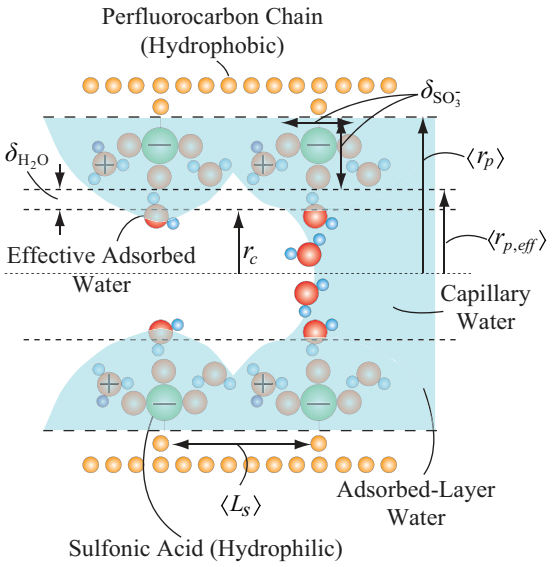

Figure 3.1: Water morphological transitions around sulfonic acid sites in small pore spacings. The pore radius r_p, effective pore radius $r_{p,eff} = r_p - \delta_{\mathrm{SO_3^-}}$, adsorbed-layer water thickness $\delta_{\mathrm{H_2O}}$, and effective adsorbed-layer water layer $r_{p,eff}$, are shown.

$$\begin{aligned}\mu &= \mu_{\rm o}(p_{g,{\rm o}},T)+\mu_{\delta_{\rm H_2O}}-v_{\rm H_2O,\mathit{l}}\frac{\sigma}{r_c}\\ &= \mu_{\rm o}(p_{g,{\rm o}},T)+v_{\rm H_2O,\mathit{l}}f(\delta_{\rm H_2O})-v_{\rm H_2O,\mathit{l}}\frac{\sigma}{r_c},\end{aligned}\tag{3.2}$$

where $\mu_{\rm o}$ is the bulk chemical potential, $p_{g,{\rm o}}$ is the bulk gas pressure, $\mu_{\delta_{\rm H_2O}}$ is the chemical potential of adsorbed-layer water, $\delta_{\rm H_2O}$ is the adsorbed-layer water thickness, σ is the surface tension of pore water, r_c is the principal radius of curvature $r_c = r_p - \delta_{\rm H_2O}$, and $v_{\rm H_2O,\mathit{l}}$ is the molar volume of the liquid water. The last two terms on the right hand side of Eq. (3.2) correspond to the surface energy change between adsorbed-layer water and Nafion. The detailed derivations are found in the previous work [82]. Assuming a cylindrical pore the morphological transition occurs at $r_c = r_{a\text{-}c}$, and we have

$$\sigma = r_c^2\frac{\partial f}{\partial r_c}|_{r_c=r_{a\text{-}c}},\tag{3.3}$$

where f is given as

$$f = -c\int\frac{1}{r^6}{\rm d}V,\quad c = 4\epsilon_{\rm LJ}\sigma_{\rm LJ}^6.\tag{3.4}$$

$\epsilon_{\rm LJ}$ is the depth of potential well, $\sigma_{\rm LJ}$ is the separation constant, and $\gamma = \pi n_f c/6$ where n_f is the number density of adsorbed water. From Eq. (3.3), the closed form solution is obtained as

$$\frac{r_p^2}{r_{\rm o}^2} = \frac{r_{a\text{-}c}^2}{r_p^2}\left(1-\frac{r_{a\text{-}c}^2}{r_p^2}\right)^{-5/2}P_{3/2}^1\left[\frac{\left(1+\frac{r_{a\text{-}c}^2}{r_p^2}\right)}{\left(1-\frac{r_{a\text{-}c}^2}{r_p^2}\right)}\right],\tag{3.5}$$

where $r_{\rm o} = (3\pi\gamma/v_{\rm H_2O,\mathit{l}}\sigma)^{1/2}$, and $P_{3/2}^1$ is the associated Legendre function.

Although a realistic Nafion pore network is complex, the homogeneous pore size assumption is used due to the criticality of the mean pore radius (predominant population). Furthermore, in operation of PEMFC, the pore surface is covered either by the adsorbed-layer or capillary water for the high proton conductivity, and this in turn minimizes the heterogeneity in surface wettability. So, the homogeneous surface wettability (force) is also assumed. Using Eq. (3.5) and the mean pore radius $\langle r_p \rangle = 2$ nm [20], the single site, nonpolarized water molecular interactions, $\varepsilon_{\mathrm{LJ}} = 15.319$ kJ/mol, and $\sigma_{\mathrm{LJ}} = 3.016$ Å [90], $\lambda_{\mathrm{H_2O},im}$ is predicted and shown in Figure 3.2. Indeed, the

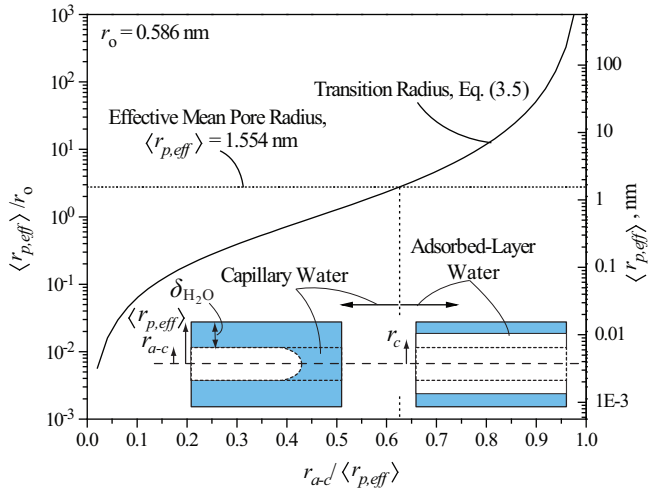

Figure 3.2: Predicted adsorbed to capillary water transition in hydrated Nafion (assumed cylindrical pore), using the morphological transition theory [82].

cubic-equivalent sulfonic acid sites make for a collective layer thickness $\delta_{\mathrm{SO_3^-}}$. Thus, the effective pore radius is reduced by $\delta_{\mathrm{SO_3^-}}$, i.e., $\langle r_{p,eff} \rangle = \langle r_p \rangle - \delta_{\mathrm{SO_3^-}} = 1.554$ nm, as shown in Figure 3.1. With this, we have $r_{a\text{-}c}/\langle r_{p,eff} \rangle = 0.63$, and we use the $r_{a\text{-}c}$ as the meniscus radius in the capillary pressure appeared in Eq. (B.2). $r_{a\text{-}c}/\langle r_{p,eff} \rangle = 0.63$ corresponds to 2 water molecules on the top of each sulfonic acid site. Also, since the pore water is locally hydrated on the sulfonic acid site, it is assumed that water

molecules are equally adsorbed on the four sides of the cubic sulfonic acid. Our preliminary MD results also show this cluster adsorption (on a homogeneous surface), and we expect that site localization is possible on heterogeneous surfaces. Considering these 4 water molecules and the additional 2 on the top, we have $\lambda_{\mathrm{H_2O},im} = 6$. Since this is close to the experimental value of $\lambda_{\mathrm{H_2O},im} = 5$ reported in [101, 18, 62], we use $\lambda_{\mathrm{H_2O},im} = 5$ as the immobile saturation (minimum saturation for capillary percolation channel), and equivalently $s_{ad,\mathrm{PE}} = 0.33$ using Eq. (C.2) and $\epsilon_{\mathrm{PE}} = 0.4$.

3.3.2 Kelvin-Cohan Theory

The capillary transition is also predicted by Kelvin-Cohan relation considering the effective capillary meniscus given as [14]

$$R_g T \ln(p_c/p_o) = -\frac{\sigma \overline{v}_{\mathrm{H_2O}}}{0.5 L_{z,p} - \delta_{\mathrm{H_2O},ad}} \tag{3.6}$$

where R_g is the gas constant, p_c is the threshold pressure of capillary condensation, σ is the surface tension, and $\overline{v}_{\mathrm{H_2O}}$ is the water molar volume.

3.4 Predicted Adsorption Isotherm

Water states (uptake) are related to the adsorption and capillary condensation in the pore network. This is explored using the molecular simulations and the proposed bimodal model. Adsorption and capillary condensation are related to the vapor pressure (number density of water molecules), temperature (kinetic energy of water

molecules), pore size (confinement), and wetting-surface heterogeneity (sulfonic acid site surface density) [21]. The water adsorption in nangaps with $L_{Z,p} = 1$ and 4 nm are calculated using the grand canonical molecular dynamics-Monte Carlo (GCMD-MC) simulation, as described in Appendix A. The snapshots of the simulated results are visualized in Figure 3.3. At low pressure $p/p_o = 0.01$, the adsorbed-water forms clusters around the sulfonic acids in both the pore sizes. At the large pore, it thickness as the pressure increases, $p/p_o = 0.3$, while at the small pore it is flooded by the capillary transition. At high pressure $p/p_o = 1$, both pores are flooded. These are consistent with the proposed water morphologies in Section 2.3.1. The predicted adsorption at $T = 300$ K and the surface sulfonic acid density $n(SO_3^-) = 1.5$, 1.75, and 2.5 nm^{-2}, are shown in Figure 3.4.

At low pressures, there is only adsorbed-water (no vapor molecules) and its thickness grows as the pressure increases. At a threshold pressure, e.g., $p/p_o = 0.95$ for $L_z = 4$ nm, 0.1 for 1 nm with $n(SO_3^-) = 1.75$ nm^{-2}, capillary condensation occurs, and the pore begins to completely fill [82]. This threshold pressure increases in the large pores, due to the weaker overlapping surface forces. However, no significant variation in this threshold pressure is found in the small pores, because of the critical confinement, therefore those are not shown in Figure 3.4. This capillary condensation is compared with the Kelvin-Cohan relation Eq. (3.6), and the Saam-Cole transition theory Eq. (3.5), using the water-water effective potential as the water-surface wall interactions beyond the Debye length. Using the bulk surface tension, the Kelvin-Cohan relation reasonably predicts the GCMD-MC results in the small pore, and shows a good agreement. However, in large pores, it predicts the GCMD-MC results

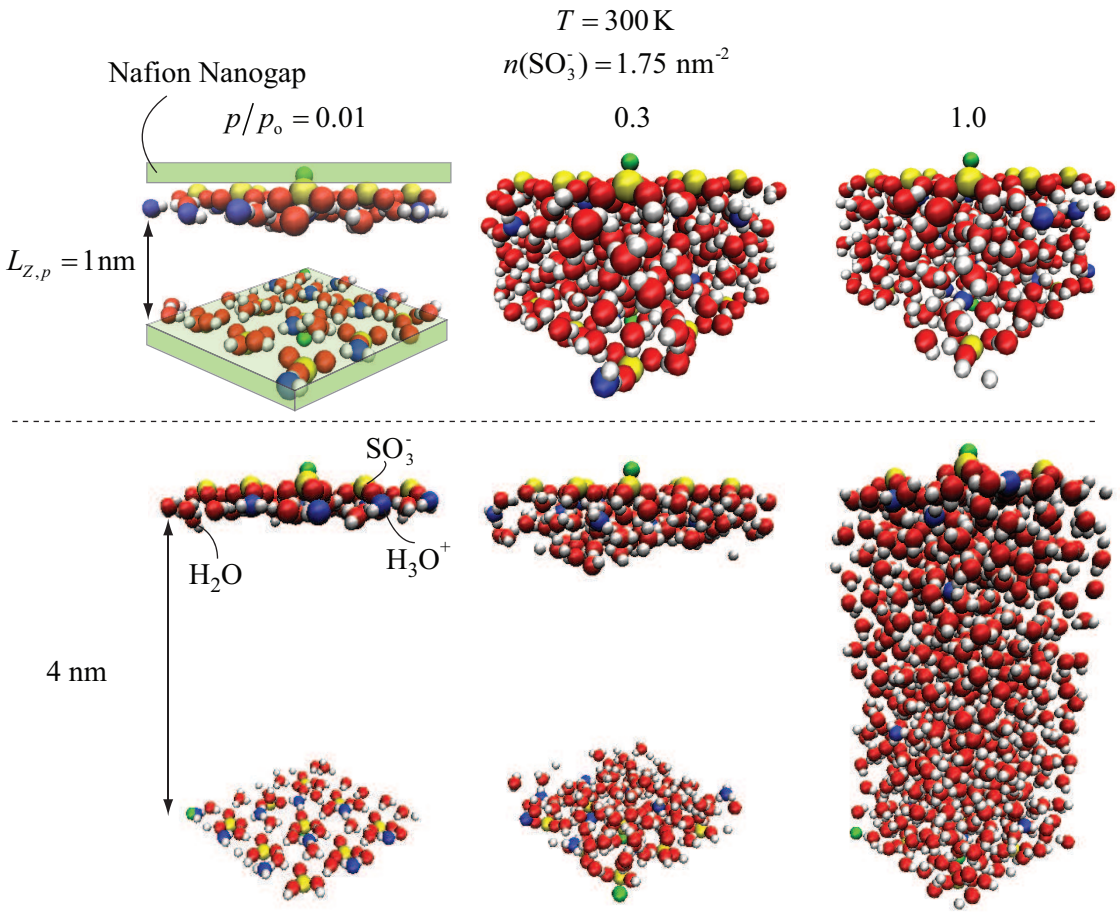

Figure 3.3: Snapshots of the adsorbed water in Nafion nanopores (nanogaps) $L_{Z,p} = 1$ and 4 nm at the reduced pressure, $p/p_o = 0.01, 0.3$, and 1.0 at $T = 300$ K and $n(SO_3^-)$ $= 1.75\ \mathrm{nm}^{-2}$ using GCMD-MC. The colors of particles represent types of atoms, sulfide (yellow), hydrogen of water (white), oxygen (red), hydrogen of hydronium (blue), and hydrophobic surface (green).

with a large sulfonic acid site density, i.e., $n(SO_3^-) = 2.5\ \mathrm{nm}^{-2}$ (hydrophilic-like, Figure 2.8), rather than the lower site density (hydrophobic-like), whereas the Saam-Cole theory predicts a delayed threshold. This is due to the large (bulk) surface tension which leads to hydrophilic-like wetting, while the effective water-water intermolecular potential tends to be weaker than the surface-water interactions. In addition, the modified BET theory Eq. (3.1) [21, 14] reasonably predicts the GCMD-MC results.

The sulfonic acid site density critically influences the adsorption and capillary

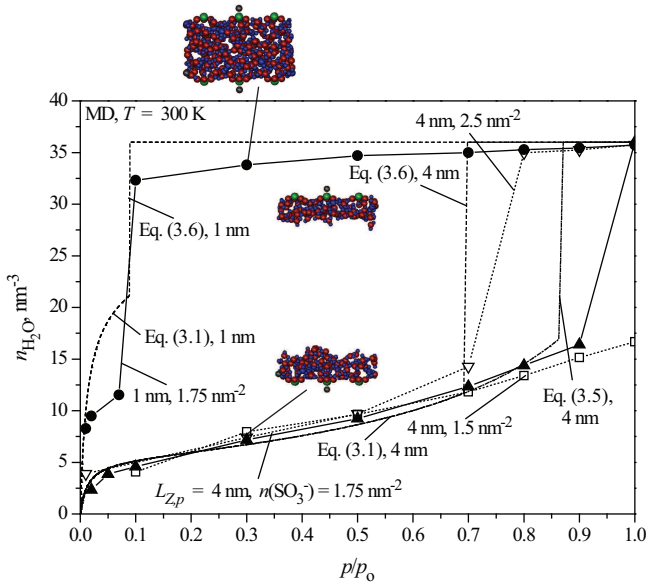

Figure 3.4: Variations of the adsorbed water in Nafion nanopores (nanogaps) $L_{Z,p}$ = 1 and 4 nm with respect to the reduced pressure, p/p_o at T = 300 K and $n(SO_3^-)$ = 1.5, 1.75 and 2.5 nm^{-2} using molecular simulation. The GCMD-MC adsorbed water is shown as insets. The predicted results using available adsorption and capillary condensation theories are also shown [82, 14, 48].

Table 3.1: Summary of various sulfonic acid surface site densities in the literature.

$n(SO_3^-)$ nm^{-2}	Comments
1.62	110 sites per 4.65 nm diameter cluster for EW = 1100 g [45]
3.3	$d_{SO_3^-\text{-}SO_3^-}$ = 0.55 nm for T = 20 to 80°C [20]
1.82	the specific surface area of 0.55 nm^2 per site [34]
0.51 to 1.23	$d_{SO_3^-\text{-}SO_3^-}$ = 0.9 to 1.4 nm for λ_{H_2O} = 4 to 15 [66]

condensation. Higher density (strong surface force, $n_{SO_3^-}$ = 2.5 nm^{-2}) increases adsorption, and the capillary condensation occurs at the lower partial pressure, whereas the lower density (weak surface force, 1.5 nm^{-2}) decreases adsorption, and the condensation is delayed without condensation at $p/p_o = 1$. We choose $n_{SO_3^-}$ = 1.75 nm^{-2} as the characteristic Nafion sulfonic acid surface density, which is in the range of reported values of 0.51 to 3.3 nm^{-2} where are summarized in Table 3.1 [45, 20, 34, 66]. The chosen site density is also based on the transport coefficients (water diffusivity

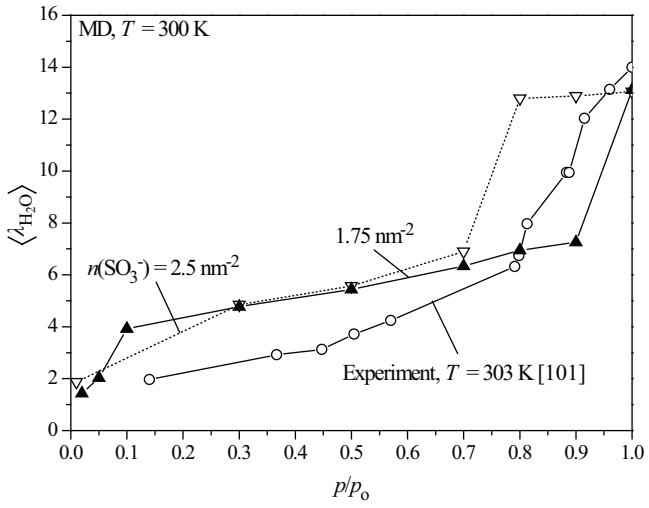

Figure 3.5: Variations of the predicted water content $\langle\lambda_{\mathrm{H_2O}}\rangle$, Eq. (3.7) as a function of the reduced pressure at $T = 300$ K. Available experimental result at $T = 303$ K is also shown [101].

and proton conductivity), especially at low pressures, and will be discussed in the following sections.

In general, the adsorbed water in Nafion is presented as water content defined by the number of water molecules per sulfonic acid site [101]. To predict the water content, $\langle\lambda_{\mathrm{H_2O}}\rangle$, the total adsorbed water amount in the bimodal pore network is calculated by integrating the GCMD-MC adsorbed water in individual pores [Figure 3.4] over the two pore sizes, as given

$$\langle\lambda_{\mathrm{H_2O}}\rangle = \frac{\sum_i n_{\mathrm{H_2O},ad} V_{L_{Z,p,i}}}{N(\mathrm{SO_3^-})}, \tag{3.7}$$

where $n_{\mathrm{H_2O},ad}$ is the number density of the adsorbed water in the individual pore, $V_{L_{Z,p,i}}$ is the pore volume for each nanogap, and $N(\mathrm{SO_3^-})$ is the total number of sulfonic acid sites. The predicted water content is shown in Figure 3.5. It is small

at low reduced pressure, $p/p_{\rm o}$, and increases with increasing pressure. At threshold pressures, $p/p_o = 0.1$ and 0.95, water adsorption significantly increases (transitions). The first transition is caused by filling the small pores $L_{Z,p} = 1$ nm, and the second is more pronounced by fully hydrating the larger pores $L_{Z,p} = 4$ nm due to significant pore volume. This agrees with the experimental result [101], especially at the large water content, while overpredicting at low pressures. It should be noted that the swelling is ignored and the pore size is chosen based on the fully humidified condition, and this causes a discrepancy especially at the low partial pressures. In addition, our model does not include hydrodynamic resistance among pores and interfacial resistance [71, 72], which in turn explains this overprediction.

3.5 Temperature-dependent Adsorption

Adsorption at elevated temperatures is important for enhanced proton conductivity, due to the increased mobility [2, 11]. The temperature-dependent adsorption for Nafion at $p/p_{\rm o} = 1$ using the modified BET, Eq. (3.1). Here, the parameters are fitted using the experimental results found in [101, 7, 44], and we have

$$\begin{aligned} \lambda_{\mathrm{H_2O},ad} &= 2.3, \\ c(T) &= \exp(\Delta E_a / k_{\rm B} T), \\ k(T) &= 1.786 - 3.194 \times 10^{-3}\ T. \end{aligned} \tag{3.8}$$

where ΔE_a is the activation energy, and predicted as 307.2 meV. The water adsorption for Nafion λ_{H_2O} at $p/p_o = 1$, is shown in Figure 3.6. The maximum $\lambda_{H_2O} = 14$ occurs at $T = 30$°C [101], and it decreases as the temperature increases. The prediction underestimates the measured datum in [44], and this is related to the sample pretreatment. Note that at $T = 80$°C, the water uptake is $\lambda_{H_2O} \simeq 7$. This is used as the thermodynamic equilibrium limit, and will be compared to the predicted liquid saturation distributions $s(z)$.

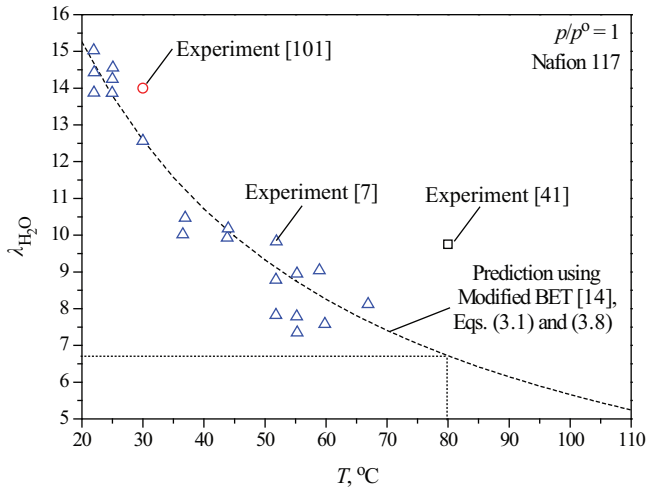

Figure 3.6: Variation of the temperature-dependent adsorption of λ_{H_2O} for Nafion 117 at $p/p_o = 1$, using the modified BET model [14] and the experimental data [101, 7, 44].

In addition, elevated temperatures constrict the network channels by drying the pores, while transport properties improve with increase in temperature. Thus, optimal operating temperature is needed. At $T = 370$ K, using the same sulfonic acid site density as at $T = 300$ K, the GCMD-MC results do not predict the available experimental results [44]. The heterogeneous ionic site distribution leads to the lateral overlapping surface forces, which in turn result in no significant temperature dependence. Thus, we suggest that the surface sulfonic acid site density and morphology

change with temperature. At high temperatures, the molecular bonds of Nafion are relaxed and then the sites are rearranged, since the bonds have moderate rotational activation energies, e.g., 91.1 to 394.6 meV [76, 77]. In addition, the pressure and temperature critically influence the mechanical properties of hydrated Nafion, i.e., viscoelasticity, by changing its pore structure, e.g., transition from the lamella to the rod-like pores when changing from $T = 300$ to 370 K at $p/p_o \sim 1$ [65]. This thermally-induced pore morphological evolution leads to low sulfonic acid densities due to increased pore surface area. Swelling, especially at high hydration, also promotes a decrease in the site density by increasing the pore surface. Overall, these combined thermal-hydration effects lead to decrease surface density, i.e., the proposed thermally-induced hydrophobicity, and we use $n_{SO_3^-} = 0.5$ nm^{-2} at $T = 370$ K with a rigid pore network. The snapshots of the simulated results are shown in Figure 3.7. The small pore is filled by the capillary transition at moderate pressure $p/p_o = 0.5$, while the large pore remains the adsorbed-water (no capillary condensation) even at the high pressure, $p/p_o = 1.0$ due to the thermally-induced hydrophobicity. Using this, the predicted adsorption decreases over the entire p/p_o at elevated temperature, as shown in 3.8(a). This decreases adsorption down to $\langle \lambda_{H_2O} \rangle = 8$ at $T = 370$ K at saturation pressure, $p/p_o = 1$, as shown in 3.8(b). The GCMD-MC results are in good agreement with the available experimental results [101, 39, 44, 7]. The suggested site density change is rather large, nearly a factor of 3, but the neglected swelling might have lead to this, which may be validated by large-scale polymer matrix simulations [97, 66].

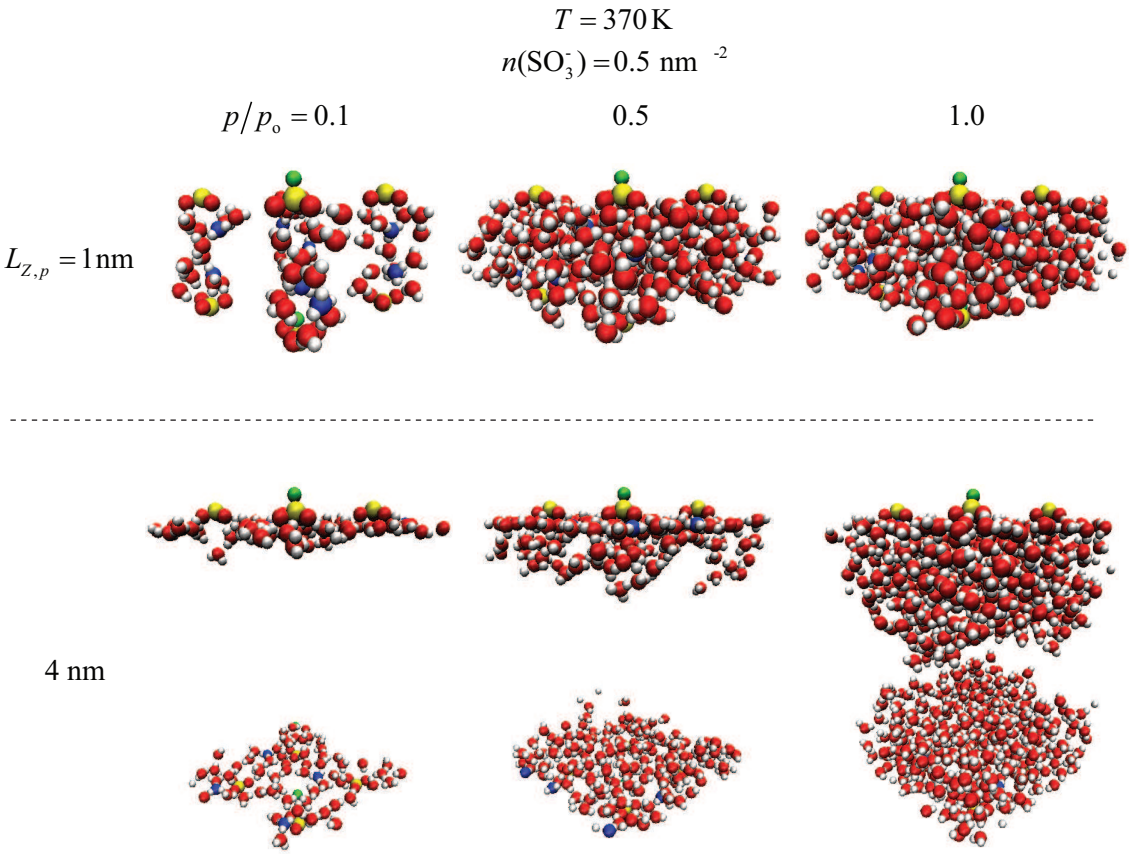

Figure 3.7: Snapshots of the adsorbed water in Nafion nanopores (nanogaps) $L_{Z,p} = 1$ and 4 nm at the reduced pressure, $p/p_\mathrm{o} = 0.1, 0.5$, and 1.0 at $T = 370$ K and $n(\mathrm{SO_3^-})$ $= 0.5\ \mathrm{nm}^{-2}$ using GCMD-MC. The colors of particles represent types of atoms, sulfide (yellow), hydrogen of water (white), oxygen (red), hydrogen of hydronium (blue), and hydrophobic surface (green).

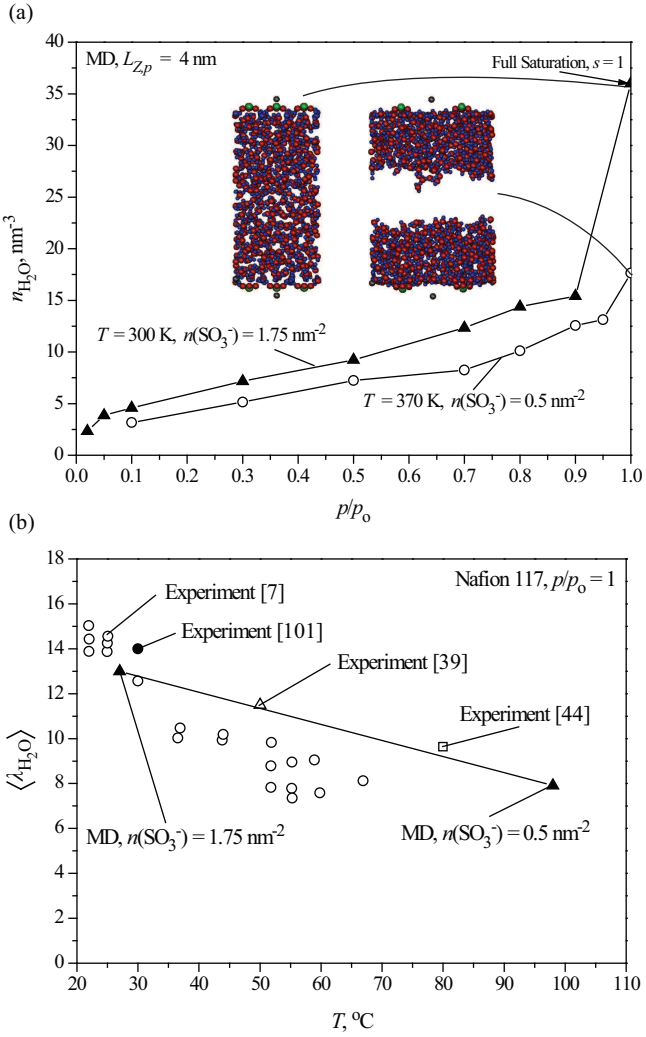

Figure 3.8: (a) Variations of the water number density in $L_{Z,p} = 4$ nm as a function reduced pressure p/p_o at $T = 300$ and 370 K. The GCMD-MC snap shots at $p/p_o = 1$ are also shown. (b) Variations of the temperature-dependent adsorption $\langle\lambda_{H_2O}\rangle$ at $p/p_o = 1$. Available experimental results are also shown [101, 39, 44, 7].

3.6 Summary

This chapter demonstrates importance of the adsorption and capillary transitions in the mesopores of the hydrated Nafion and their effects on the water uptake (adsorption isotherm) as well as water/proton transport. It is shown that the bimodal model succeeds in predicting the measured water uptake and its transitions at the room temperature and high pressures, while the water adsorption in the individual pores is predicted using GCMD-MC. At elevated temperatures, the thermally-induced hydrophobicity of Nafion is proposed, and it leads to the observed delay in capillary transition at high pressures. This explains the decreased adsorption and lack of jumps in the transport properties, and will be further discussed in Chapters 4 and 5.

Chapter 4

Water Self Diffusion

4.1 Introduction

Water self-diffusion is an important transport property of the hydrated Nafion, especially when it is equilibrated with a vapor reservoir. This property is critically related to the Nafion hydration, showing a monotonic increase as a function of increased water content $\langle \lambda_{H_2O} \rangle$ with a transition at $\langle \lambda_{H_2O} \rangle \simeq 5$ to 6, $T = 300$ K. In this chapter, the molecular dynamic simulation-based bimodal model is used to predict the water self diffusion and explain its transitions.

4.2 MD Predicted Results and Discussions

Water self diffusion through the adsorbed phase occurs in the pore network, and the effective self diffusion is predicted using the molecular simulation combined with the bimodal model, as shown in Figure 4.1. The diffusivity, D_{H_2O} through the ad-

sorbed water in $L_{Z,p} = 1$ and 4 nm is calculated using the Green-Kubo autocorrelation Eq. (A.2) at $T = 300$ K as a function of p/p_o, and the results are reported in Table 4.1. Then, the effective diffusivity $\langle D_{H_2O} \rangle$ is calculated using the predicted adsorption (Figure 3.4) and 30×30, the 2-D bimodal network as depicted in Figure 1.2. Calculation details are given in our previous work [52]. The results for $T = 370$ K are not shown here, and the temperature dependency in the diffusivity will be discussed below.

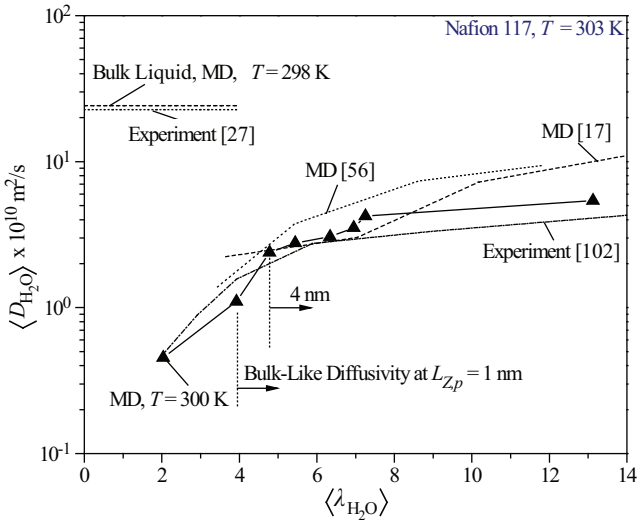

Figure 4.1: Variations of water self-diffusion coefficient in Nafion as function of average water content, at 303 K. The experiential results [102] and the available MD results [56, 17], are also shown along with the experimental result for bulk liquid water at T = 298 K [27].

At $\langle \lambda_{H_2O} \rangle \sim 2$ ($p/p_o \sim 0.05$), the effective diffusivity is significantly reduced compared to that in bulk liquid water, due to the significantly reduced diffusion within the thin adsorbed layers (Debye screening length). At $\langle \lambda_{H_2O} \rangle \sim 4$ ($p/p_o \sim 0.1$), there is a significant increase in diffusivity approaching bulk behavior dominated by capillary condensation in the small pores. At $\langle \lambda_{H_2O} \rangle \sim 5$ ($p/p_o \sim 0.3$), the adsorbed

Table 4.1: MD predicted D_{H_2O}, as a function of p/p_o and $\langle\lambda_{H_2O}\rangle$ at $T = 300$ K for $L_{Z,p} = 1$ and 4 nm.

p/p_o ($\langle\lambda_{H_2O}\rangle$)	D_{H_2O}, m^2/s at $L_{Z,p} = 1$ nm	D_{H_2O}, m^2/s at $L_{Z,p} = 4$ nm
0.05(2.0)	5.70×10^{-10}	5.82×10^{-10}
0.1(3.9)	1.21×10^{-9}	7.64×10^{-10}
0.3(4.8)	1.25×10^{-9}	2.13×10^{-9}
0.5(5.4)	1.27×10^{-9}	2.25×10^{-9}
0.7(6.3)	1.29×10^{-9}	2.45×10^{-9}
0.8(6.9)	1.29×10^{-9}	3.03×10^{-9}
0.9(7.2)	1.30×10^{-9}	3.20×10^{-9}
1.0(13.1)	1.29×10^{-9}	2.80×10^{-9}

layers in large pores grow beyond the screening length. For $\langle\lambda_{H_2O}\rangle > 5$, there is further filling of the large pores. These results are in good agreement with experiments [102] and available MD results [56, 17]. Our large scale, bimodal pore-network treatment gives better predictions compared to the full atomistic simulations [56, 17]. Swelling decreases $\langle\lambda_{H_2O}\rangle$ for $\langle\lambda_{H_2O}\rangle < 5$ [Figure 3.4(b)], and with swelling, the predictions are further close to the experiment. For a validation, our MD predicted bulk liquid diffusivity at $T = 298$ K is in excellent agreement with the existing experiment [27].

4.3 Summary

Water self-diffusion is explored using the molecular dynamic simulation based bimodal model, and the results show a good agreement with the measured water self diffusion compared to the available full molecular simulations [56, 17]. The model explains that the transition is related to the capillary condensation and the resulting bulk-like diffusion in both the pore sizes. It also reveals that the diffusion is significantly hindered in the small pores due to large water-surface interactions, and it

gradually increases with the hydration of the large pores towards the maximum self diffusion. The diffusion is also related to the proton conductivity through hydronium diffusion, and it will be discussed in the next chapter. The temperature-dependent diffusion is also discussed there.

Chapter 5

Proton Transport

5.1 Introduction

Good proton transport is a key transport feature of the hydrated Nafion, and is known to be through the hydrogen-bond network. Then the proton conductivity is critically related to the pore-water morphology and increases with respect to the water content $\langle \lambda_{H_2O} \rangle$ with a jump at $\langle \lambda_{H_2O} \rangle \simeq 5$ to 6, $T = 300$ K. In this chapter, the molecular dynamic simulation-based bimodal model is used to predict the translational hydronium diffusion and explain its transition jumps.

5.2 Proton Conductivity: Capillary-Transition Related Jump

Considering the morphological transitions, the measured water content and proton conductivity [101] are analyzed, as shown in Figure 5.1. The general discussions are

omitted, and here we emphasize key features, i.e., roles of morphological transitions. Criticality of three morphological transitions are appeared in the onset of the proton conductivity by adsorbed-layer water transition at $\lambda_{\mathrm{H_2O},ad} = 2.3$ ($s_{ad,\mathrm{PE}} = 0.18$), in the proton conductivity jump by capillary water transition at $\lambda_{\mathrm{H_2O},im} = 5$ ($s_{im,\mathrm{PE}} = 0.33$), and in further jump by Schröder paradox at $\lambda_{\mathrm{H_2O}} = 14$ ($s_{im,\mathrm{PE}} = 0.78$). Considering

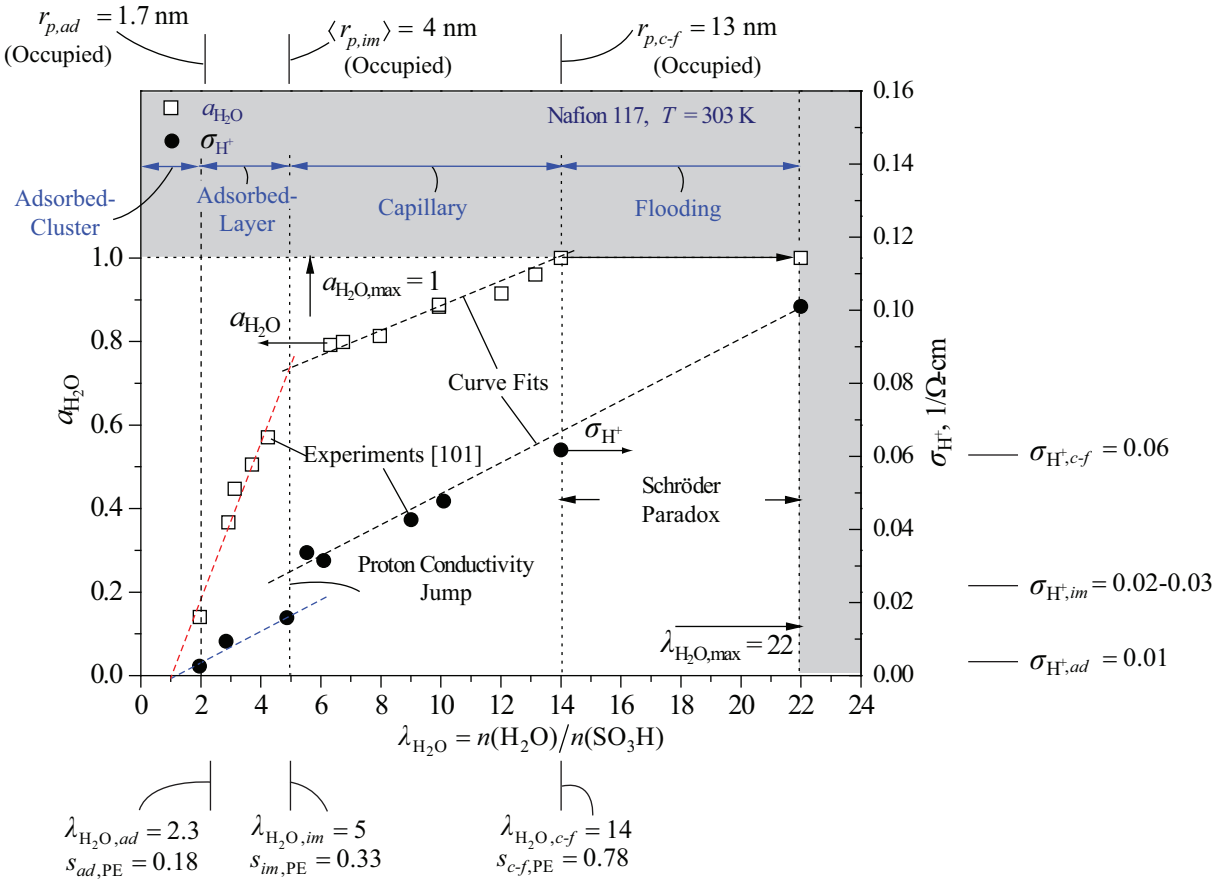

Figure 5.1: Measured water content $\lambda_{\mathrm{H_2O}}$ and proton conductivity $\sigma_{\mathrm{H^+}}$, as a function of water activity $a_{\mathrm{H_2O}}$ for Nafion 117 at $T = 303$ K [101]. Three morphological transitions are indicated, and the corresponding, filling pore size r_p are also shown. Onset of the adsorbed-layer $\lambda_{\mathrm{H_2O},ad} = 2.3$ [36, 101, 14], proton conductivity jump at $\lambda_{\mathrm{H_2O},im} = 5$ [101, 14, 18] are shown. Maximum water content $\lambda_{\mathrm{H_2O},max} = 22$, and water activity $a_{\mathrm{H_2O},max} = 1$ are also shown.

the morphological transitions, a modified proton conductivity $\sigma_{\mathrm{H^+}}(s, T)$ is proposed

as a function of the water content, using experimental results in [101]. With the Arrhenius relation for the temperature dependence [88], we have

$$\begin{aligned}
\sigma_{H^+}(\lambda_{H_2O}, T) &= 0, \quad \lambda_{H_2O} < 2.3 \\
\sigma_{H^+}(\lambda_{H_2O}, T) &= [0.0074(\lambda_{H_2O} - 2.3)] \exp\left[1,268\left(\frac{1}{303.2} - \frac{1}{T}\right)\right], \\
&\quad \lambda_{H_2O} < 5 \\
\sigma_{H^+}(\lambda_{H_2O}, T) &= [0.0041(\lambda_{H_2O} - 5.0) + 0.030] \exp\left[1,268\left(\frac{1}{303.2} - \frac{1}{T}\right)\right], \\
&\quad \lambda_{H_2O} \geq 5. \qquad (5.1)
\end{aligned}$$

This modified relation is used in Eqs. (B.1) and (B.2), and the liquid saturation distribution $s(z)$ and cell performance curve are given in the following sections.

5.3 Nernst-Einstein Relation

In bulk liquid water, proton primarily transfers via Grotthuss (or hopping) diffusion, i.e., proton hops over a hydrogen-bond network of water molecules, which is fast and dominant [22, 106, 1, 68, 67], whereas in the Nafion pore network, the strong surface forces (Debye length) critically hinder the transport. Thus, no significant Grotthuss diffusion is considered within the Debye length, and the surface-force hindered translational hydronium diffusion is included. Using Nernst-Einstein relation [10, 11], we have

$$\sigma_{H^+} = \frac{e^2_{H^+}}{k_B T}(n_{H_3O^+} D_{H_3O^+,D} + n_{H^+} D_{H^+,G}) \qquad (5.2)$$

where e_{H^+} is the proton charge, n_{H^+} is the number density of proton for the Grotthuss diffusion, $n_{H_3O^+}$ is the number density of hydronium for the translational diffusion, $D_{H^+,G}$ is the Grotthuss diffusivity, and $D_{H_3O^+,D}$ is the translational diffusivity.

5.4 MD Predicted Results and Discussions

$D_{H_3O^+,D}$ is calculated using MD-simulated, 8-18 hydroniums and the Green-Kubo autocorrelation relation Eq. (A.2), as presented in Table 5.1 and 5.2. The Grotthuss diffusivity is calculated using the available relaxation time for rotations of water molecules [2, 10, 11]. At $T = 300$ K, $D_{H^+,G} = 7\times10^{-9}$ m^2/s, using $D_{H^+,G} = d^2_{O\text{-}O}/6\tau_D$, and morphological rearranging relaxation time $\tau_D = 1.5$ ps, and O-O distance 0.255 nm in $H_9O_4^+$ [2], and at $T = 370$ K, $D_{H^+,G} = 11\times10^{-9}$ m^2/s, using $\tau_D = 1.0$ ps. For the proton number density, EW = 1100 g/mol, and 2 g/cm^3 are used. When the adsorbed water layer is beyond the screening length, $n_{H^+}/(n_{H^+}+n_{H_3O^+}) = 0.5$ is assumed. We note that this population density ratio is so far not confirmed, even with the recent microscopic analyses and *ab initio* molecular dynamics simulations[22, 106, 1, 68, 67].

Table 5.1: MD predicted $D_{H_3O^+,D}$, as a function of p/p_o and $\langle\lambda_{H_2O}\rangle$ at $T = 300$ K for $L_{Z,p} = 1$ and 4 nm.

p/p_o ($\langle\lambda_{H_3O^+}\rangle$)	$D_{H_3O^+}$, m^2/s at $L_{Z,p} = 1$ nm	$D_{H_3O^+}$, m^2/s at $L_{Z,p} = 4$ nm
0.05(2.0)	3.89×10^{-11}	3.65×10^{-11}
0.1(3.9)	2.25×10^{-10}	9.60×10^{-11}
0.3(4.8)	2.38×10^{-10}	2.62×10^{-10}
0.5(5.4)	3.07×10^{-10}	3.13×10^{-10}
0.7(6.3)	3.58×10^{-10}	3.58×10^{-10}
0.8(6.9)	4.29×10^{-10}	3.69×10^{-10}
0.9(7.2)	4.90×10^{-10}	1.22×10^{-9}
1.0(13.1)	5.25×10^{-10}	1.51×10^{-9}

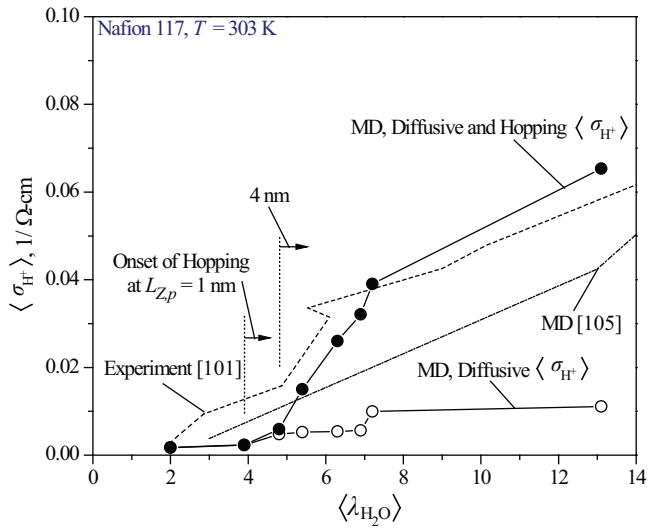

Figure 5.2: Variations of the MD predicted proton conductivity including the jumps caused by capillary condensation and bulk-like diffusivity at $T = 300$ K. The predicted translational-diffusion proton conductivity, and the available experimental [101] at $T = 303$ K and MD results [105] at $T = 298$ K are shown.

Using the proposed bimodal network, (30×30, 2-D network as visualized in Figure 1.2) and the Kirchhoff law at the pore junctions [14], the effective conductivity $\langle \sigma_{H^+} \rangle$ is calculated as a function of the water content $\langle \lambda_{H_2O} \rangle$, as shown in Figure 5.2.

At $\langle \lambda_{H_2O} \rangle < 2$, the proton conductivity is negligibly small, because the adsorbed water is mainly within the screening length. As the pressure increases, the small hydrophilic-like pores readily fills at $\langle \lambda_{H_2O} \rangle \sim 4$, and the proton conductivity significantly increases through bulk-like proton diffusion and hopping. However, in the large hydrophobic-like pores, the conductivity is still hindered, which in turn causes no significant proton conductivity jump. At $\langle \lambda_{H_2O} \rangle \sim 8$, the adsorbed water layers in the large pores grow beyond the screening length, and the bulk-like diffusion and hopping result in significant enhancement. At high pressures, capillary condensation occurs and leads to the maximum conductivity. The diffusive proton conductivity

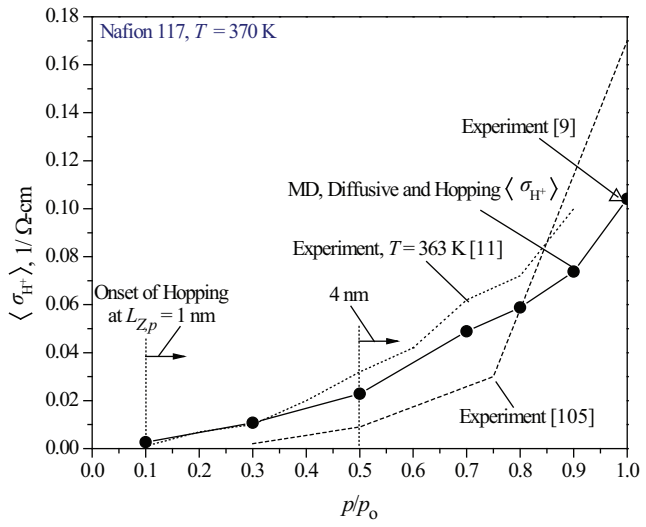

Figure 5.3: Variations of the MD predicted proton conductivity including the jumps caused by capillary condensation and bulk-like diffusivity at $T = 370$ K. The experimental results at $T = 373$ K are also shown [11, 9, 105].

Table 5.2: MD predicted $D_{H_3O^+,D}$, as a function of p/p_o at $T = 370$ K for $L_{Z,p} = 1$ and 4 nm.

p/p_o	$D_{H_3O^+}$, m^2/s at $L_{Z,p} = 1$ nm	$D_{H_3O^+}$, m^2/s at $L_{Z,p} = 4$ nm
0.1	8.72×10^{-10}	2.86×10^{-9}
0.3	8.12×10^{-10}	2.92×10^{-9}
0.5	1.04×10^{-9}	3.10×10^{-9}
0.7	2.18×10^{-9}	3.25×10^{-9}
0.8	2.52×10^{-9}	5.43×10^{-9}
0.9	3.01×10^{-9}	5.53×10^{-9}
1.0	4.15×10^{-9}	7.01×10^{-9}

is also shown, indicating that its contribution is nearly one third. An available MD result is also shown, and it underestimates the proton conductivity since the hopping is not properly considered [105].

At the elevated temperatures as shown in Figure 5.3, there is a decrease in adsorption due to the proposed thermally-induced hydrophobicity, while there are increases in translational and rotational diffusivity. Overall, the proton conductivity increases, however, no capillary condensation occurs in the large pores, resulting in no pro-

ton conductivity jump. The existing experimental results show inconsistency among them, and this may be caused by the different polymer structural changes at elevated temperatures, induced by different thermal histories and fabrication processes [11, 9, 105], while the predictions show a reasonable agreement with the experiments.

5.5 Summary

The proton conductivity is explored by using the monomodal model and the molecular dynamic simulation-based bimodal model, and by addressing the pore-water morphologies and their transitions. The monomodal model predicts that the proton conductivity jump is caused by the adsorbed-water to capillary condensation. This jump is further explained by the MD-based bimodal network model, showing that the capillary condensation results in the bulk-like translational and the rotational proton diffusion in both pore sizes. These show that the proton transport is significantly hindered in the small pores [due to large water-surface interactions (Debye length)] and gradually increases with the flooding of the large pores (reaches the bulk maximum). At elevated temperatures, the capillary transition is delayed due to the thermally-induced hydrophobicity and results in lack of any transition jumps.

Chapter 6

Capillary Flow Throughout and Resulting Performance

6.1 Introduction

The pore water of hydrated Nafion is represented by the water content λ_{H_2O} (ratio of the number of adsorbed water molecule to the number of sulfonic acid site [101]), or by the liquid saturation s (fraction of pore volume occupied by liquid water [94, 96]). The water content, λ_{H_2O} and liquid saturation, s are related through the porosity and the molar volume [93]. λ_{H_2O} is used for the proton and water diffusion models [88], whereas s is used for the hydrodynamic water models [94, 93].

In normal cell operations, i.e., $T < 90^oC$ and RH = 100%, Nafion contacts with liquid water in the adjacent porous layers, i.e., CLs and GDLs [95, 96, 43, 48, 72], and the liquid water pressure should be continuous across the Nafion interfaces. Since MD simulations show no significant water vapor at $p/p_o < 1$ due to very high Knudsen

number, we postulate that the water vapor transport is negligible, and the liquid water transport is the primary water flow mechanism.

6.2 Liquid Saturation Distribution

6.2.1 Monomodal wetting

The pore-water distribution throughout PEMFC are predicted using the hydrodynamic model for $T = 80°\text{C}$ and $j_e = 0.75$ A/cm^2, and are compared with the experimental results [43], as shown in Figures 6.1(a) and (b). The measured water volume [43] is represented as the liquid saturation $s(z)$ in Figure 6.1(a) and water content $\lambda_{\text{H}_2\text{O}}(z)$ in Figure 6.1(b), assuming no swelling of Nafion and the reduced porosity of each layer due to the expected mechanical compression in PEMFC (Table B.1) and Eqs. (Eq. C.1) and (Eq. C.2) in Appendix A. The prediction of $s(z)$ shows the maximum liquid saturation at the cathode side of Nafion where water is produced there, while $s(z)$ decreases towards both anode and cathode channels, showing that the liquid water transport by capillary pressure gradient. The predictions show a reasonable agreement to the experiment with maximum liquid saturation of $s(z) \sim 0.35$, with overestimation by nearly 100% in all the layers. This discrepancy of the lowered liquid water measurement may be due to the large measurement uncertainty at high spatial resolution (~ 16.4 μm), or unknown material/geometrical parameters used in the predictions [93]. Regardless, this prediction using the low immobile saturation $s_{im,\text{PE}} = 0.33$ or $\lambda_{\text{H}_2\text{O},im} = 5$ results in better agreement with the experiment,

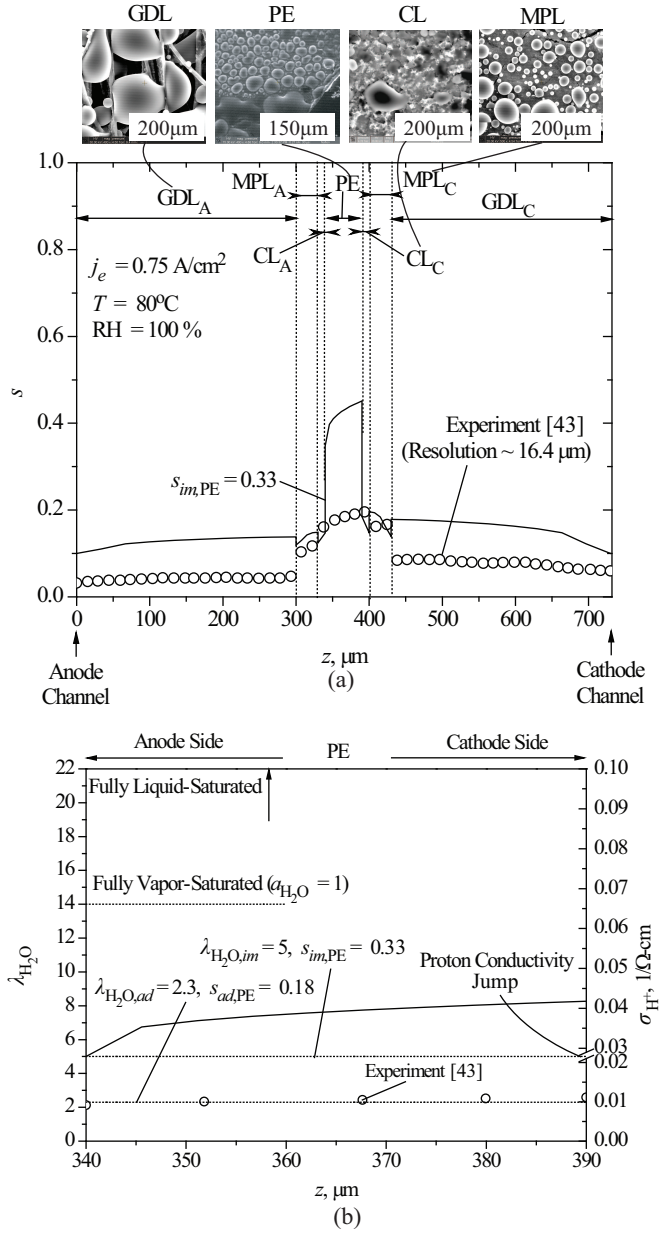

Figure 6.1: (a) Spatial distribution of the predicted liquid saturation, and comparison with the experiment [43] throughout PEMFC. (b) Based on predicted and measured liquid saturation from (a), the distribution of water content, and variation of proton conductivity are shown for Nafion.

compared to the previous study (high $s_{im,\mathrm{PE}} = 0.78$ or $\lambda_{\mathrm{H_2O},im} = 14$ at the Schröder paradox) [93].

To further demonstrate the pore water in Nafion, the distribution of water content $\lambda_{\mathrm{H_2O,PE}}(z)$, and proton conductivity are shown in Figure 6.1(b). The measured water content increases from the anode to cathode side, even though it is nearly constant $\lambda_{\mathrm{H_2O,PE}}(z) \sim 2$ which is close to $\lambda_{\mathrm{H_2O},ad}$. These low liquid saturations seems to be too low for required proton conductivity, i.e., $\lambda_{\mathrm{H_2O},im} = 5$ (or $s_{im,\mathrm{PE}} = 0.33$). Here, as discussed, using required liquid saturation at the anode side, $s_{im,\mathrm{PE}} = 0.33$, monotonically increasing $s(z) > s_{im,\mathrm{PE}}$ up to $\lambda_{\mathrm{H_2O,PE}}(z) \simeq 8$ is obtained. This maximum water content is similar to the thermodynamic, equilibrium maximum [Eq. (3.8)].

Therefore, the proposed capillary pore-water percolation model with low $\lambda_{\mathrm{H_2O},im}$ appears plausible and explains the measured low liquid saturation. Moreover, no high water content of the Schröder paradox is necessary to have a good proton conductivity. In addition, the inverse tree-like percolation channels model in GDLs and MPLs [52] are also supported by this low liquid saturation distribution.

Note that we assume nonswelling Nafion for the sake of simplicity of analysis and then compare with the predictions by available experimental water sorption data with swelling Nafion. However, the proposed thermodynamic equilibrium limit shows only as high as $\lambda_{\mathrm{H_2O}} \sim 7$ which is not enough to make a significant difference in water sorption and membrane structure by swelling. In addition, the nonswelling membrane would allow for lower water sorption than the swelling membrane, where is still bounded by the thermodynamic equilibrium limit. Thus, our prediction of low $\lambda_{\mathrm{H_2O}}$ (high operating temperature) is still plausible.

6.2.2 Bimodal wetting

The capillary pressure in the adjacent layers is positive due to their hydrophobicity. The capillary pressure continuity leads to fully-hydrated hydrophilic-like (small) pores in Nafion, whereas it results in partially-filled hydrophobic-like (large) pores (due to the smaller capillary meniscus) compatible with the adjacent layers, as shown in Figure 6.2(a). Thus, the liquid water flows through the percolated network channel by the small pores, whereas it meanders around the partially-filled (adsorbed water only) large pores since the adsorbed water is immobile [54]. This immobile saturation is calculated using the Debye length. Liquid flow through the small pores is calculated using the Hagen-Poiseuille relation, while the proton transport is allowed in all the pores. The water flow rate in the Nafion pore network must be continuous throughout the layers, and the flow rate in the adjacent layers is calculated using our previous model [48]. This is used as the boundary conditions for the bimodal water-wetting network to predict the capillary (liquid) pressure and the required liquid saturation distribution.

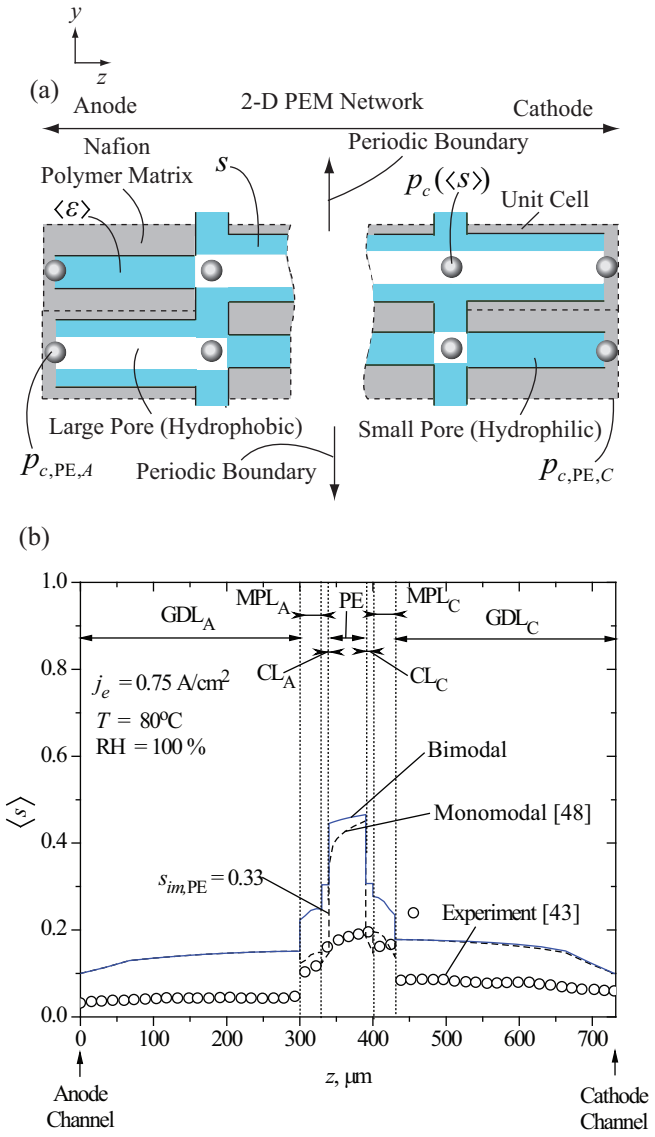

Figure 6.2: (a) Schematic of the 2-D, bimodal water-wetting pore network. (b) The predicted liquid saturation distribution within Nafion and its adjacent layers in a fuel cell assembly corresponding to the available experimental conditions and results [43]. The available prediction using hydrophobic-homogeneous treatment [48] is also shown for comparison.

A constant vapor pressure throughout the layers is assumed. Using this prescribed water flow rate and electrical current density, the capillary pressure is calculated using the Onsager relation given as [95, 55]

$$\begin{aligned}
\boldsymbol{j}_e &= \left[-\sigma_{\mathrm{H^+}}(s)\nabla\varphi_e - \frac{\sigma_{\mathrm{H^+}}(s)\alpha_{\mathrm{eo}}}{\mathrm{F}}\overline{v}_{\mathrm{H_2O}}\nabla p_c(s)\right], \\
\dot{\boldsymbol{m}}_{\mathrm{H_2O},l} &= \frac{1}{M_{\mathrm{H_2O}}}\left\{-\frac{\sigma_{\mathrm{H^+}}(s)\alpha_{\mathrm{eo}}}{\mathrm{F}}\nabla\varphi_e \right. \\
&\quad \left. - \left[\frac{\pi M_{\mathrm{H_2O}}\rho_l r_p^4}{8\mu_l\overline{v}_{\mathrm{H_2O}}} + \frac{\sigma_{\mathrm{H^+}}(s)\alpha_{\mathrm{eo}}^2}{\mathrm{F}^2}\right]\overline{v}_{\mathrm{H_2O}}\nabla p_c(s)\right\}, \\
\nabla\cdot\boldsymbol{j}_e &= 0, \\
\nabla\cdot\dot{\boldsymbol{m}}_{\mathrm{H_2O},l} &= 0,
\end{aligned} \tag{6.1}$$

where j_e is the electrical current density, $\sigma_{\mathrm{H^+}}(s)$ is the proton conductivity, α_{eo} is the electro-osmotic coefficient, $p_c(s)$ is the capillary pressure, $\dot{m}_{\mathrm{H_2O},l}$ is the superficial liquid water flux rate, ρ_l is the liquid water density, μ_l is the viscosity of liquid water, $M_{\mathrm{H_2O}}$ is the molar mass of water, and $\overline{v}_{\mathrm{H_2O}}$ is the water molar volume. The electro-osmotic coefficient $\alpha_{e,o} = 1$ [98, 31] is used. It should be noted that adsorbed water (partially filled pores) also has a condensed-phase pressure, i.e., disjoining pressure [8, 55], but the volume-average capillary pressure is used here [54].

Using the predicted capillary pressure, the resulting local liquid saturation $s_{L_{Z,p,i}}$ is calculated by the van Genuchten capillary pressure model Eq. (B.6) [37, 48], and the volume average liquid saturation $\langle s\rangle$ is predicted using the given relation as

$$\langle s\rangle = \frac{\sum_i s_{L_{Z,p,i}} V_{L_{Z,p,i}}}{\sum_i V_{L_{Z,p,i}}}. \tag{6.2}$$

It should be noted that the small, hydrophilic-like pore population ratio is 0.53 and its volume ratio is 0.22, and the minimum saturation is $\langle s \rangle = 0.37$ using fully-saturated small pores and 1.5 adsorbed-water layer (Debye screening length) as an immobile saturation in the large pores. Using $T = 80$°C, $p = 2.4$ atm, and $j_e = 0.75$ A/cm^2 [43], the bimodal wetting results are presented in Figure 6.2(b), overpredicting the hydrophobic-homogeneous model results [48], while underpredicting the liquid-equilibrated model results [93]. The predicted results also overestimate the available experiment [43], and this is caused by rather low measured liquid saturation due to the measurement uncertainties. More detailed discussions on this discrepancy are provided in our previous work [93, 48]. The maximum liquid saturation is limited by the capillary pressure continuity, and will be less than one, while the minimum liquid saturation is the immobile saturation in the large pores, which in turn is related to the Debye length.

6.3 Cell Performance

Figure 6.3 shows the predicted cell performances using Eq. (B.1) and comparisons with the available experimental results, for $T = 80$°C [43]. The measured electrical potential $\Delta\varphi_e$ drops sharply at the low current density regime, $j_e = 0$ to 0.25 A/cm^2, mainly due to the activation loss for the limited reaction rate, while it linearly decreases due to the ohmic loss (limited proton conductivity) at moderate current density regime, $j_e = 0.25$ to 0.75 A/cm^2. This shows that the proposed, proton conductivity [Eq. (5.1)] predicts the moderate ohmic loss. At moderate and high

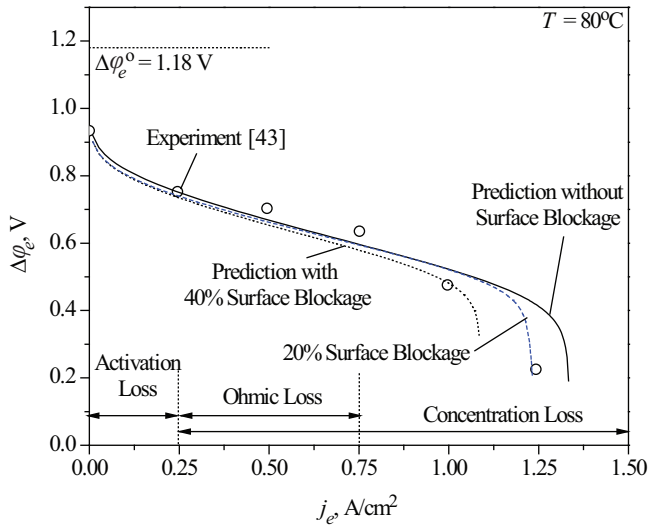

Figure 6.3: Variation of the predicted cell potential as a function of current density at $T = 80^{o}$C, and comparison with experimental results [43]. Predictions for 20 and 40 % surface blockage are also shown. Activation, ohmic, and concentration losses regimes are also indicated.

current densities, $j_e = 0.25$ to 1.25 A/cm^2, limited oxygen supply causes a significant reduction in $\Delta\varphi_e$. The predictions do not match the experiments at high current densities, and one possible reason is an additional oxygen diffusion resistance by the surface droplet as addressed in Appendix B. The performance is also predicted considering a 40% surface coverage and reduces the maximum current density by 18%. Other possible reasons may be our one-dimensional treatment of the liquid saturation in GDL (but oxygen diffusion treatment is two dimensional), and the liquid saturation jumps at the interfaces e.g., Eq. (B.7). Further improvements can be made by considering two-dimensional liquid saturation, by improving the liquid saturation jumps at these interfaces as suggested in [41], by considering available thermal model [92], and extensive GDL mechanical compression ratio (45% compression ratio allows for nearly 25-35% decrease in the maximum available current density at $\Delta\varphi_e = 0.3$

V) [33].

6.4 Optimal Pore-Water State

The optimal pore-water state of the hydrated Nafion requires capillary-network channels for high proton conductivity and for effective back-capillary flow. Neither dry nor flooding Nafion is desirable, since the first limits the proton conductivity and the latter results in excess hydration of CLs, hindering fuel supplies. In the pore-size distribution, the increased number of the small, hydrophilic-like pores would result in high liquid saturation (or high water content), while it would lead to reduced water/proton transport due to the pore confinement within the Debye screening distance. However, increase in the number of large hydrophobic-like pores causes low hydration and this either enhances transport due to decreased confinement or hinders it due to presence of thin adsorbed-layer water only. With a different sulfonic acid surface density, this optimal pore-water content also changed. Thus, the ideal polymer electrolyte should have an optimal pore-size distribution (including confinement) for ideal wetting properties, and so far other than Nafion, has been a fabrication challenge.

6.5 Summary

The capillary liquid flow and the resulting liquid saturation and their effects on the cell performance are predicted using the mono- and bimodal wetting models. The

predictions show a reasonable agreement with the available, yet limited, experimental results [43]. The bimodal model predicts a slightly higher saturation distribution than the monomodal model due to full saturation in small, hydrophilic pores. In the monomodal model, the capillary transition leads to the onset of the liquid flow. In contrast, in the bimodal model liquid dominantly flows through the network channels of the smaller, hydrophilic-like pores, while remaining immobile in the large, hydrophilic-like pores. The optimal pore-water states related to the water/proton transport aspects are also discussed.

Chapter 7

Conclusions

7.1 Contributions

This study examines the atomic-level pore-water states and water/proton transport in the Nafion mesopores and uses a pore-network model to predict wetting and transport phenomena within it. For the atomic-level study, the molecular simulation, i.e., GCMD-MC is used for water adsorption and capillary transition, water self diffusivity, and the resulting proton conductivity. For the pore network, mono- and bimodal pore-size/water-wetting treatments are developed to investigate the effective pore-water states and water/proton transport. This combined approach makes it possible to understand the wetting/transport physics and explain capillary condensation, monotonically increasing water self diffusivity, and proton conductivity jump all observed in experiments.

This research primarily relies on theoretical approach through numerical simulations. However, our SAXS data and the available experimental results are used

intensively to validate the proposed models and to clarify assumptions that are made. Challenges in both numerical simulation and experimental results are to extract useful information of interest, which needs to be compiled into a uniform framework. Therefore, analytic, theoretical modeling is used here to minimize this gap.

Significant contributions of this work are summarized below:

- *Development of MD-based, bimodal, water-wetting model for a unified treatment.* We proposed Nafion bimodal pore-size (confining and nonovelapping surface forces, based on the Debye screening length) and water-wetting (hydrophilic and hydrophobic-like) pore network based on molecular simulation and SAXS results. We used a solid polymeric backbone for a unified treatment of the hydrated Nafion pore water states and its water-related proton transport. This model predicts the capillary condensation in adsorption and proton conductivity including their jumps, and the capillary liquid flow and saturation distribution with proper liquid pressure continuity with the adjacent layers. The predicted liquid saturation distribution is higher than that using the homogeneous hydrophobic wetting (monomodal) model, which is caused by the full saturation in the hydrophilic pores.

- *Development of simple, homogeneous water-wetting model, emphasizing pore-water morphological transitions.* Four pore-water states and three morphological transitions are proposed for the pore network-channel in hydrated Nafion. Criticality of the transitions on proton conductivity and hydraulic pore water transport are discussed, while addressing Nafion pore-size distribution and the

Schröder paradox. We find that the first transition is related to the onset of proton conductivity, the second leads to the onset of the capillary percolation channels and proton conductivity jump at $\lambda_{\mathrm{H_2O},im} = 5$, using the pore-water morphology transition theory [82]. Using this as immobile saturation, the predicted water distribution $s(z)$ shows a reasonable agreement with the measurement [43]. We also find that the third transition is related to the paradox, postulating further capillary advancing, which allows for the thermodynamic equilibrium limit, i.e., temperature- dependent adsorption at full vapor saturation. These transitions appear in the experimental pore-size distribution which shows capillary percolation channel sizes. Based on these transitions, the optimal Nafion pore water content is found to be in between the second and third transition, i.e., capillary-percolation mechanism.

- *Suggestion of thermally-induced hydrophobic wetting surface for significantly decreasing adsorption at elevated temperature.* We suggest thermally-induced hydrophobic mesopore surface (reduced sulfonic acid density) due to low rotational threshold barrier and relaxed intermolecular interactions, i.e., flexible backbone. This results in delayed capillary transition, and in turn leads to decreasing adsorption at elevated temperatures. Using the modified BET [14], a temperature-dependent adsorption is also predicted and shows that this limits the maximum water content on the cathode side of Nafion.

- *Explanations of roles of pore- or domain-size-dependent confinement on water wetting and its resulting proton transport.* It is found that the smaller domains

are readily water filled and also retarding the transport due to the surface force overlap. The larger domains are sensitive to the surface forces, temperature, and pressure, and contribute significantly to transport despite being partially water filled.

7.2 Proposed Future Work

There are three extensions of the current study that should be pursued:

- Atomic-level study for pore-water in hydration/temperature-dependent backbone is necessary to understand wetting evolution in pore surface structural changes and resulting transport alteration. Both experimental approaches and full atomic simulations have challenges due to its complex chemical structure and low degree of crystallinity. A large scale simulation, i.e., coarse grain approach [97, 66] may reveal realistic hydrated pore wetting evolutions as a function of vapor pressure and temperature.

- Identifying the role of Nafion side chains (sulfonic acid) on proton conduction is needed to understand its atomic-level behavior. In this study, it is assumed that there is no significant proton transport within the Debye screening length, i.e., classically strong intermolecular interactions. However, fundamentals of proton transport kinetics in presence of external charges are not clear enough to optimize the Nafion chemical/mechanical properties. This can be examined by *ab initio* or *ab inito*-MD including quantum aspects, and the result can lead to further optimization of the Nafion backbone structure and sulfonic acid

density.

- Water distribution in Nafion, under static and fuel cell operation, needs to be further experimentally investiaged with high resolution. The enhanced fuel cell design requires optimal hydration throughout all layers, and the theoretical studies primarily rely on many assumptions to predict the optimal liquid saturation. Accurate water distribution measurement will help in the understanding the role of liquid water and in future direction of the fuel cell water management research.

7.3 Outlook

Theoretical work is essential for insight into the nature of physical phenomena, especially where it is not readily measurable. However, it can never replace experimental research. Experiments make no assumption, and new and innovative physical phenomena are always observed in the experiments. However, experimental work also has inherent challenges, i.e., it is not a direct tool to explain a phenomenon and sometimes it does not yield direct useable information. The combinational approach using both theory and experiment leads to synergetic benefits from both sides.

Appendix A

Grand Canonical Molecular Dynamics - Monte Carlo Simulation

Water adsorption and water/proton transport are predicted using the GCMD-MC [89]. Nafion pore is represented as two infinite, parallel slabs (usfing periodic boundary conditions in the x and y directions) separated by a physical width, L_z [87], as shown in Figure 2.6 (a). We assume that the surfaces are uncorrugated, stationary, and rigid (no swelling). Hydrophobic surface is modeled by 1-D Lennard-Jones potential, whereas the hydrophilic sites are represented by SO_3^- only [87]. The numbers of the sites per pore are 8 to 18 for $T = 300$ and 370 K to represent $n(SO_3^-) = 1.75$ and 0.5 nm^{-2}. These ionized pores are neutralized by the same same number of hydroniums. The modified simple polarization charge extended (MSPC/E) water is

used [15]. This water potential is superior to SPC, and SPC/E which is for vapor-liquid equilibria at $T = 300.15$ to 582.28 K, relevant to adsorption. An equal number of hydroniums are added to electrically neutralize the sulfonic acid system using an available potential [60]. The chemical potential and the vapor pressure are calculated using a virial expansion [89, 40], and the second order virial coefficient is used [5]. The leapfrog Verlet algorithm [30] is used to solve the Newton equation and the SHAKE algorithm is used for the rigid molecules [81], and the temperature is controlled by Brendsen thermostat [6]. The long-range electrostatic force is calculated by the pair-wise additive method [28], where the damping coefficient, $\alpha = 0.2$ Å^{-1}, and cutoff r_c = 1.2 nm are used. The simulation temperatures are $T = 298$ to 370 K. The time step $\Delta t = 0.5$ fs is used for a time integration, and the total simulation time is 1.5 to 3 ns, until there is no significant change in the water molecule population, <5% for 1 ns. This method is validated by testing bulk vapor/liquid water at $T = 300$ and 370 K [15]. With controlled chemical potentials, the MD predicted pressures agree with the ideal gas pressure for vapor and available simulation results for liquid water [15].

The isosteric heat of adsorption is calculated using [73]

$$\Delta h_{lg,ad} = -\frac{\langle \varphi N \rangle - \langle \varphi \rangle \langle N \rangle}{\langle N^2 \rangle - \langle N \rangle^2} + k_{\mathrm{B}} T \tag{A.1}$$

where φ is the system potential energy and N is the number of particle in the nanopore.

The self-diffusion coefficient D_i for species i in the individual pore is calculated

using the Green-Kubo autocorrelation relation given as [55],

$$D_i = \lim_{\tau \to \infty} \int_0^{\tau} \mathrm{d}t \langle u_i(t) u_i(0) \rangle, \tag{A.2}$$

where i is either water or hydronium, t and τ are times, $u_i(t)$ is the velocity of the species i from MD results. Since the species i in nanogap diffuses only in x- and y-directions, x- and y-direction velocity profiles are used for the average diffusivity. $\tau = 100$ ps is used, which is two orders of magnitude larger than the diffusion time which is 0.5 ps at $T = 370$ K.

Appendix B

Mathematical Formulation of Water Transport throughout PEMFC

We propose a capillary-hydrodynamic model for pore-water in Nafion. Whereas, the previous mathematical models [52, 53] are used in CLs, MPLs, and GDLs to predict liquid saturation distribution $s(z)$ throughout PEMFC. Figure Figure B.1 shows a schematic drawing of percolation channel including ESEM image of water on each layer surface as well as key mathematical formulations with transport parameters. Fuel cell performance $\Delta\varphi_e - j_e$ is also predicted using the predicted $s(z)$ and the relation given as [63]

$$\Delta\varphi_e \;=\; \Delta\varphi_e^{\mathrm{o}} - \Delta\varphi_{e,o} - \Delta\varphi_{e,a} - \Delta\varphi_{e,c}$$

$$= \Delta\varphi_e^{\mathrm{o}} - \int \frac{j_e}{\sigma_{\mathrm{H}^+}(s)}\mathrm{d}z - \frac{RT}{2\mathrm{F}}\ln\left(\frac{j_e}{j_{e,\mathrm{o}}}\right) + k_c \ln\left(\frac{p_{\mathrm{H}_2}^2 p_{\mathrm{O}_2}}{p_{g,\mathrm{H}_2\mathrm{O}}^2}\right), \qquad \text{(B.1)}$$

where $\Delta\varphi_e^{\mathrm{o}}$ is the reversible electro-chemical potential ($\Delta\varphi_e^{\mathrm{o}} = 0.18$ V at $T = 80^{\mathrm{o}}$C [74]), $\Delta\varphi_{e,\mathrm{o}}$ is the ohmic loss, $\Delta\varphi_{e,a}$ is the activation loss, and $\Delta\varphi_{e,c}$ is the concentration loss, $j_{e,\mathrm{o}}$ is the exchange current density, $\sigma_{\mathrm{H}^+}(s)$ is the proton conductivity, R is the ideal gas constant, T is the temperature in CL, F is the Faraday constant, k_c is the concentration loss constant, and p_{H_2}, $p_{\mathrm{H}_2\mathrm{O}}$, and p_{O_2} are the partial pressure of the hydrogen, vapor, and oxygen in CLs respectively. Considering the electro-osmotic flow driven by proton transport and back-capillary flow from anode to cathode, the Onsager relation is given as [95, 55]

$$\begin{aligned}
\boldsymbol{j}_e &= \left[-\sigma_{\mathrm{H}^+}(s)\nabla\varphi_{e,o} - \frac{\sigma_{\mathrm{H}^+}(s)\alpha_{\mathrm{eo}}}{\mathrm{F}}\overline{V}_{\mathrm{H}_2\mathrm{O}}\nabla p_c(s)\right], \\
\dot{\boldsymbol{m}}_{\mathrm{H}_2\mathrm{O},l} &= \frac{1}{M_{\mathrm{H}_2\mathrm{O}}}\left\{-\frac{\sigma_{\mathrm{H}^+}(s)\alpha_{\mathrm{eo}}}{\mathrm{F}}\nabla\varphi_{e,o}\right. \\
&\quad \left. - \left[\frac{\rho_l M_{\mathrm{H}_2\mathrm{O}} K K_{rl}(s)}{\mu_l \overline{V}_{\mathrm{H}_2\mathrm{O}}} + \frac{\sigma_{\mathrm{H}^+}(s)\alpha_{\mathrm{eo}}^2}{\mathrm{F}^2}\right]\overline{V}_{\mathrm{H}_2\mathrm{O}}\nabla p_c(s)\right\}, \\
\nabla\cdot\boldsymbol{j}_e &= 0, \\
\nabla\cdot\dot{\boldsymbol{m}}_{\mathrm{H}_2\mathrm{O},l} &= 0, \qquad \text{(B.2)}
\end{aligned}$$

where j_e is the electrical current density, $S_r(s)$ is the reduced saturation, $\sigma_{\mathrm{H}^+}(s)$ is the proton conductivity, α_{eo} is the electro-osmotic coefficient, $p_c(s)$ is the capillary pressure, $\dot{m}_{\mathrm{H}_2\mathrm{O},l}$ is the superficial liquid water mass flux rate, ρ_l is the liquid water density, K is the absolute permeability, $K_{rl}(s)$ is the relative permeability, μ_l is the viscosity of liquid water, and $M_{\mathrm{H}_2\mathrm{O}}$ is the molar mass of water. The electro-osmotic

coefficient $\alpha_{e,o} = 1$ [31] is used since we emphasize on $\lambda_{\mathrm{H_2O}}(z) < 14$. The local liquid water mass flux by capillary pressure is given as [54]

$$\dot{\boldsymbol{m}}_{\mathrm{H_2O},l} = -\frac{\rho_l K K_{rl}}{\mu_l}\nabla p_c = -\frac{\rho_l K K_{rl}}{\mu_l}(\frac{\mathrm{d}p_c}{\mathrm{d}S_r})\nabla S_r, \tag{B.3}$$

where S_r is the reduced saturation

$$S_r(s) = \frac{s - s_{im}}{1 - s_{im}}, \tag{B.4}$$

and s_{im} is the immobile saturation. $s_{im,\mathrm{PE}} = 0.33$ at the anode side of Nafion as discussed in Section 3.3, while $s_{im,i} = 0.1$ is used for all the other layers [52]. $K_{rl}(s)$ is the relative permeability, and we use [54]

$$K_{rl}(s) = S_r(s)^3. \tag{B.5}$$

For the capillary pressure, the van Genuchten model is used as [54, 37]

$$p_c = \frac{\sigma \cos\theta_c}{(K/\epsilon)^{1/2}}\left[S_r(s)^{n/1-n} - 1\right]^{1/n}, \tag{B.6}$$

where $n = 3.56$ for GDL (Toray 090) [37]. Parameter n influences the capillary pressure gradient, and becomes sensitive to n where the saturation is close to the immobile saturation. Since Nafion is overall hydrophobic (similar to GDL from ESEM observations), we use $n = 3.56$ for Nafion.

Capillary pore-water in Nafion continuously connects with percolation channels

in the adjacent layers, i.e., CLs, MPLs, and GDLs, thus liquid pressure is expected to be continuous. In general, the continuous liquid pressure is satisfied with the liquid saturation jump where layer pore-size is mismatched [52, 53]. However, the liquid pressure continuity may not be satisfied especially at a large pore-size mismatched interface as observed using X-ray (nearly doubled liquid saturation jump at the interface) [41]. Moreover, the liquid pressure is not continuous across the boundaries where the pore size is vastly different [53], i.e., water oozing out of small pores is independent of the liquid pressure in the large pores to which it flows. Here, we use the doubled saturation jump condition,

$$S_{r,f}|_{+} = \frac{1}{2} S_{r,c}|_{-}, \tag{B.7}$$

where the subscript f and c corresponds to the fine and coarse media, respectively, and the subscripts $+$ and $-$ are the interfaces facing towards GC and Nafion, respectively.

In CLs, it is assumed that vapor water is produced by the electrochemical reaction on the cathode side, and no evaporation/condensation are allowed on both sides as shown in Figure B.1. The water mass transport is conserved in CLs, and the given reactant mass flow rate for electrochemical reaction are given as

$$\dot{m}_{\mathrm{H_2},A} = M_{\mathrm{H_2}} \frac{j_e}{2F}, \quad \dot{m}_{\mathrm{O_2},C} = -M_{\mathrm{O_2}} \frac{j_e}{4F}. \tag{B.8}$$

In CLs and MPLs, the one-dimensional effective diffusion model is used [52], whereas a two-dimensional diffusion analysis is made in GDLs. At the interfaces between

GDLs and GCs, the channel ribs (landings) block the passages of water and fuels. This impermeable interface causes a decrease in the species diffusion through GDL (due to the increased diffusion path). On the permeable GDL surface (outside of landing areas), we consider a surface-convective resistance for oxygen supply. Thus, Maxwell-Stephen equation for oxygen diffusion is solved in two dimensions with the impermeable boundary conditions under the channel ribs (L_{ch} = 1 mm and L_{rib} = 1 mm), and periodic boundary condition along y direction. However, we used an averaged (along y direction) liquid saturation, since no significant variation is found in the experimental results at $T = 80^{o}$C [43]. Further gas diffusion resistance results from blockage by surface water droplets on the GDL surface, shown in [32, 58]. These droplets hinder interfacial oxygen transport, especially at high current densities, and cause a significant concentration loss. The surface droplets form by oozing of water out of GDL and by condensing vapor in the gas channel, and are intermittently sheared away by the channel gas flow. Thus, the extent of droplet coverage is transient and here we assume an average of 40% surface coverage based on the visualization reported in [58], in turn increasing the impermeable portion of the interface (in addition to the landing areas). We place this blockage in between the landing areas (Figure B.1). The parameters used to solve the governing equations are listed in Tables B.1 and B.2.

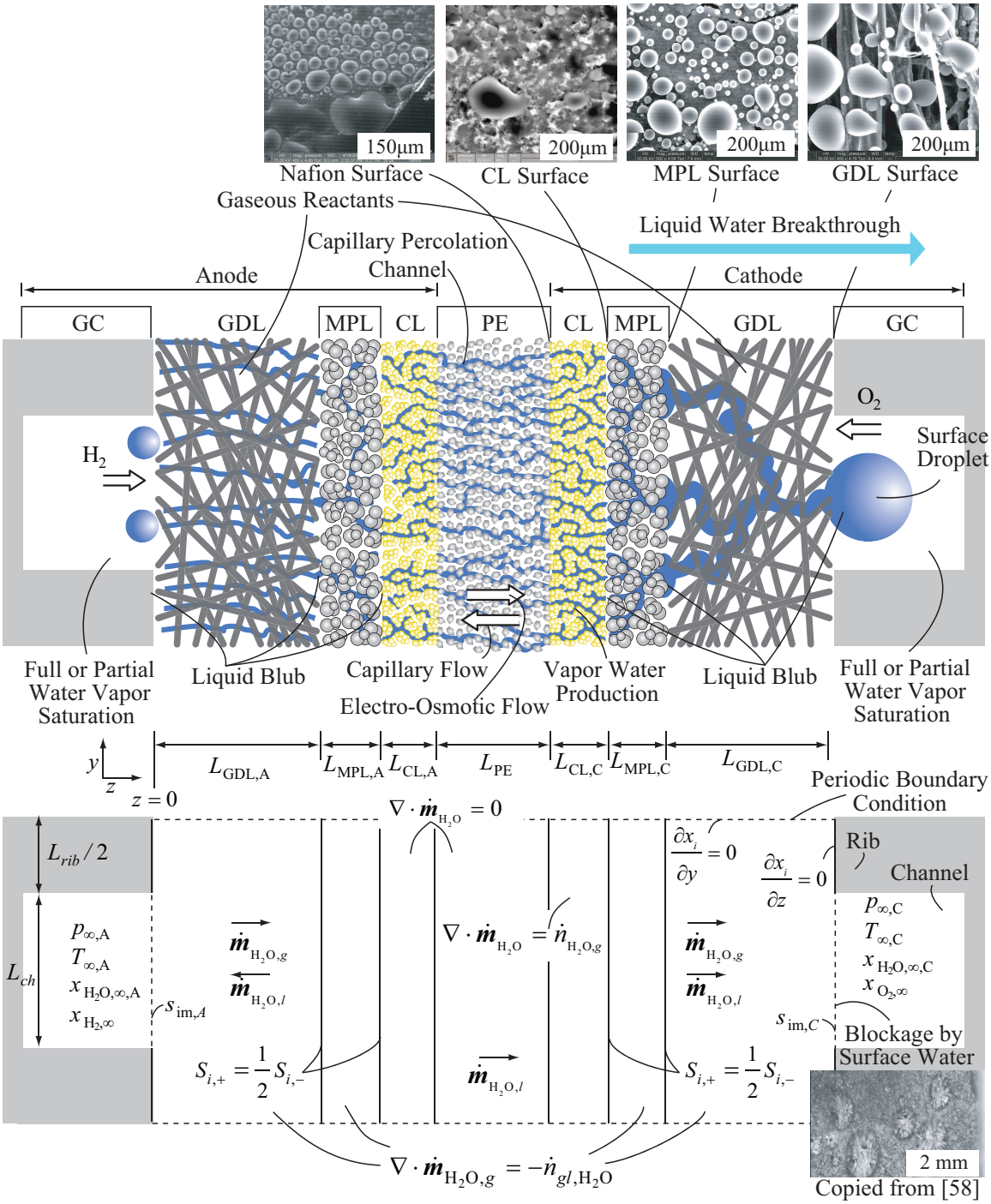

Figure B.1: Schematic of pore-water states in PE (Nafion), CL, MPL, GDL, and GC porous layers, and their layer thicknesses. Hydrogen and oxygen supplies, capillary and electro-osmotic liquid water flows, water production by the electrochemical reaction, and percolation throughout all the layers are also shown. ESEM images of water on PE (Nafion), MPL, GDL surfaces are also shown. The list of transport parameters, boundary conditions and surface droplet image on GDL reproduced by permission from the authors [58] are also shown.

Table B.1: Layer properties used in the models.

Layer	Parameter	Description	Magnitude
Nafion	K	absolute permeability	1.8×10^{-18} m^2 [95]
	$\theta_{c,\mathrm{PE}}$	contact angle	110°
	r_c	principal radius of curvature	1.3 nm
	$s_{\mathrm{im,PE}}$	immobile saturation	0.33
	ϵ_{PE}	porosity	0.25 (reduced)
	L_{PE}	layer thickness Nafion 112	50 μm
CL	K	absolute permeability	2×10^{-16} m^2 [53]
	$\theta_{c,\mathrm{CL}}$	contact angle	145°
	$s_{\mathrm{im,CL}}$	immobile saturation	0.1
	ϵ_{CL}	porosity	0.25 (reduced)
	L_{CL}	layer thickness	10 μm
MPL	K	absolute permeability	8×10^{-14} m^2 [53]
	$\theta_{c,\mathrm{MPL}}$	contact angle	130°
	$s_{\mathrm{im,MPL}}$	immobile saturation	0.1
	ϵ_{MPL}	porosity	0.3 (reduced)
	L_{MPL}	layer thickness	30 μm
GDL	K	absolute permeability	8.3×10^{-12} m^2 [37]
	$\theta_{c,\mathrm{GDL}}$	contact angle	120°
	$s_{\mathrm{im,GDL}}$	immobile saturation	0.1
	ϵ_{GDL}	porosity	0.6 (reduced)
	L_{GDL}	layer thickness	300 μm

Table B.2: Parameters used in the prediction.

Parameter	Description	Magnitude
$D_{m,\mathrm{O_2}}$	oxygen diffusivity	30.3 $\mathrm{mm^2/s}$
$D_{m,\mathrm{H_2}}$	hydrogen diffusivity	114 $\mathrm{mm^2/s}$
$D_{m,\mathrm{H_2}O}$	vapor diffusivity	34.5 $\mathrm{mm^2/s}$
$j_{e,\mathrm{o}}$	exchange current density	1 $\mu\mathrm{A/cm^2}$
k_c	concentration loss constant	0.04 V
L_{ch}	width of channel	1 mm
L_{rib}	width of channel rib (landing)	1 mm
p	pressure	2.4 atm
T	temperature	80°C
$v_{\mathrm{H_2O},l}$	molar volume of water	1.8×10^{-5} $\mathrm{m^3/mole}$
$x_{\mathrm{O_2},\infty}$	oxygen mole fraction	0.168
$x_{\mathrm{H_2},\infty}$	hydrogen mole fraction	0.80
$x_{\mathrm{H_2O},\infty}$	vapor mole fraction	0.20
α_{eo}	electro-osmotic coefficient	1
$\Delta\varphi_e^{\mathrm{o}}$	maximum reversible voltage	1.18 V [74]
μ_l	viscosity of liquid water	0.000405 kg/m-s
σ	surface tension	0.0644 N/m

Appendix C

Relation between Water Content and Liquid Saturation

The occupying liquid pore-water volume ratio is represented as the variation of the water content λ_{H_2O} given as [93]

$$\frac{V_{H_2O,l}}{V_p + V_{PE}} = \frac{\lambda_{H_2O} v_{H_2O}}{v_{PE} + \lambda_{H_2O} v_{H_2O}} \tag{C.1}$$

where $V_{H_2O,l}$ is the liquid water volume in the pore, V_p is the pore volume, v_{PE} is the molar volume of Nafion, v_{H_2O} is the molar volume of water. Using Eq. (C.1), the liquid saturation s is given as [54]

$$s = \frac{V_{H_2O,l}}{V_p} = \frac{\lambda_{H_2O} v_{H_2O}}{\epsilon_{PE}(v_{PE} + \lambda_{H_2O} v_{H_2O})} \tag{C.2}$$

where ϵ_{PE} is the porosity of Nafion.

Appendix D

Average Pore Radius

The average pore radius $\langle r_p \rangle$ is estimated as [20]

$$\langle r_p \rangle = \frac{1}{V_{\mathrm{H_2O},l,max}} \int_{r_{p,min}}^{r_{p,max}} (\frac{\mathrm{d}V_{\mathrm{H_2O},l}}{\mathrm{d}r_p}) r_p \mathrm{d}r_p, \tag{D.1}$$

where r_p is the pore radius, $V_{\mathrm{H_2O},l}$ is the liquid water volume. In [20], $r_{p,min} = 1$ nm and $r_{p,max} = 1000$ nm are used.

Bibliography

[1] N. Agmon. The grotthuss mechanism. *Chem. Phys. Lett.*, 244:456–462, 1995.

[2] N. Agmon. Tetrahedral displacement: The molecular mechanism behind the Debye relaxation in water. *J. Phys. Chem.*, 100:1072–1080, 1996.

[3] F. Barbir. *PEM Fuel Cells*. Elsevier Academic Press, 2005.

[4] M. Bass and V. Freger. Hydration of Nafion and Dowex in liquid and vapor environment: Schroeder's paradox and microstructure. *Polymer*, 49:497–506, 2008.

[5] K.M. Benjamin, J.K. Singh, A.J. Schultz, and D.A. Kofke. Higher-order virial coefficients of water models. *J. Phys. Chem. B*, 111:11463–11473, 2007.

[6] H.J.C. Berendsen, J.P.M. Postma, W.F. Van Gunsteren, A. Dinola, and J.R. Haak. Molecular-dynamics with coupling to an external bath. *J. Chem. Phys.*, 81:3684–3690, 1984.

[7] K. Broka and P. Ekdunge. Oxygen and hydrogen permeation properties and water uptake of Nfion 117 membrane and recast film for PEM fuel cell. *J. Appl. Electrochem.*, 27(2):117–123, 1997.

[8] V.P. Carey. *Statistical Thermodynamics and Microscale Thermophysics*. Cambridge University Press, 1999.

[9] M. Casciola, G. Alberti, M. Sganappa, and R. Narducci. On the decay of Nafion proton conductivity at high temperature and relative humidity. *J. Power Sources*, 162:141–145, 2006.

[10] P. Choi and R. Datta. Sorption in proton-exchange membranes: An explanation of Schroeder's paradox. *J. Eelectrochem. Soc.*, 150(12):E601–E607, 2003.

[11] P. Choi, N.H. Jalani, and R. Datta. Thermodynamics and proton transport in Nafion II. Proton diffusion mechanisms and conductivity. *J. Eelectrochem. Soc.*, 152(3):E123–E130, 2005.

[12] L.H. Cohan. Sorption hysteresis and the vapor pressure of concave surfaces. *J. Am. Chem. Soc.*, 60(2):433–435, 1938.

[13] N. Cornet, G. Beaudoing, and G. Gebel. Influence of the structure of sulfonated polyimide membranes on transport properties. *Separation and Purification Technology*, 22-23:681–687, 2001.

[14] P. Costamagna, S. Grosso, and R. Di Felice. Percolative model of proton conductivity of Nafion membranes. *J. Power Sources*, 178(2):537–546, 2008.

[15] G.C. Coulougouris, I.G. Economou, and D.N. Theodorou. Engineering a molecular model for water phase equilibrium over a wide temperature range. *J. Phys. Chem. B*, 102:1029–1035, 1998.

[16] T.R. Crompton. *Battery Reference Book*. Newnes, 2000.

[17] S.T. Cui, J.W. Liu, M.E. Selvan, D.J. Keffer, B.J. Edwards, and W.V. Steele. A molecular dynamics study of a Nafion polyelectrolyte membrane and the aqueous phase structure for proton transport. *J. Phys. Chem.*, 111:2208–2218, 2007.

[18] S. Deodar and P. Luner. Water in polymers. page 273, Washington, DC, 1980. ACS Symposium Series.

[19] O. Diat and G. Gebel. Proton channels. *Nat. Mater.*, 7:13–14, 2008.

[20] J. Divisek, M. Eikerling, V. Mazin, H. Schmitz, U. Stimming, and Yu.M. Volfkovich. A study of capillary porous structure and sorption properties of Nafion proton-exchange membranes swollen in water. *J. Eelectrochem. Soc.*, 145(8):2677–2683, 1998.

[21] D.D. Do. *Adsorption Analysis: Equilibria and Kinetics*. Imperial College Press,, 1998.

[22] M. Eigen. Proton transfer, acid-base catalysis, and enzymatic hydrolysis. *Angew. Chem. Int. Edit.*, 3(1):1–72, 1964.

[23] M. Eikerling and A.A. Kornyshev. Proton transfer in a single pore of a polymer electrolyte membrane. *J. Elecroanal. Chem.*, 502:1–14, 2001.

[24] M. Eikerling, A.A. Kornyshev, and A.R. Kucernak. Water in polymer electrolyte fuel cells: Friend or foe? *Phys. Today*, 59:38–44, Oct. 2006.

[25] M. Eikerling, A.A. Kornyshev, and E. Sphor. Proton-conducting polymer electrolyte membranes: Water and structure in charge. *Adv. Polym. Sci.*, 215:15–54, 2008.

[26] M. Eikerling, A.A. Kornyshev, and U. Stimming. Electrophysical properties of polymer electrolyte membranes: A random network model. *J. Phys. Chem. B*, 101:10807–10820, 1997.

[27] D. Eisenberg and W. Kauzmann. *The Structure and Properties of Water*. Oxford University Press, London, 1969.

[28] C.J. Fennell and J.D. Gezelter. Is the Ewald summation still necessary? pairwise alternatives to the accepted standard for long-range electrostatics. *J. Chem. Phys.*, 124:234104, 2006.

[29] V. Freger. Elastic energy in microscopically phase-separated swollen polymer networks. *Polymer*, 43:71–76, 2002.

[30] D. Frenkel and B. Smit. *Understanding Molecular Simulation: from Algorithms to Applications, 2nd Ed.* Academic Press, 2002.

[31] T. Fuller and J. Newman. Experimental determination of the transport number of water in Nafion 117 membrane. *J. Eelectrochem. Soc.*, 139(5):1332–1337, 2003.

[32] F.Y. Zhang, X.G. Yang, and C.Y. Wang. Liquid water removal from a polymer electrolyte fuel cell. *J. Eelectrochem. Soc.*, 153(2):A225–A232, 2006.

[33] J. Ge, A. Higier, and H. Liu. Effect of gas diffusion layer compression on PEM fuel cell performance. *J. Power Sources*, 159:922–927, 2006.

[34] G. Gebel. Structural evolution of water swollen perfluorosulfonated ionomers from dry membrane to solution. *Polymer*, 41:5829–5838, 2000.

[35] G. Gebel, O. Diat, S. Escribano, and R. Mosdale. Water profile determination in a running PEMFC by small-angle neutron scattering. *J. Power Sources*, 179:132–139, 2008.

[36] T.D. Gierke, G.E. Munn, and F.C.J. Wilson. The morphology in Nafion perfluorinated membrane products, as determined by wide- and small-angle x-ray studies. *J. Polym. Sci.*, 19(11):1687–1704, 1981.

[37] J.T. Gostick, M.W. Fowler, M.A. Ioannidis, M.D. Pritzker, Y.M. Volfkovich, and A. Sakars. Capillary pressure and hydrophilic porosity in gas diffusion layers for polymer electrolyte fuel cells. *J. Power Sources*, 156:375–387, 2006.

[38] S. Goswami, S. Klaus, and J. Benziger. Wetting and absorption of water drops on Nafion films. *Langmuir*, 24:8627–8633, 2008.

[39] X. Guo, J. Fang, K. Tanaka, H. Kita, and K. Okamoto. Synthesis and properties of novel sulfonated polyimides from 2,2'-bis(4-aminophenoxy)biphenyl-5,5'-disulfonic acid. *J. Polym. Sci., Part A: Polym. Chem.*, 42(6):1432–1440, 2004.

[40] J.-P. Hansen and I.R. McDonald. *Theory of Simple Liquids, 3rd Ed.* Academic Press, 2006.

[41] C. Hartnig, I. Manke, R. Kuhn, N. Kardjilov, J. Banhart, and W. Lehnert. Cross-sectional insight in the water evolution and transport in polymer electrolyte fuel cells. *Appl. Phys. Lett.*, 92:134106, 2008.

[42] H.-G. Haubold, Th. Vad, H. Jungbluth, and P. Hiller. Nano structure of Nafion: a SAXS study. *J. Phys. Chem. B*, 46:1559–1563, 2001.

[43] M.A. Hickner, N.P. Siegel, K.S. Chen, D.S. Hussey, D.L. Jacobson, and M. Arif. In situ high-resolution neutron radiography of cross-sectional liquid water profiles in proton exchange membrane fuel cells. *J. Eelectrochem. Soc.*, 155(4):B427–B434, 2008.

[44] J.T. Hinatsu, M. Mizuhata, and H. Takenaka. Water uptake of perfluorosulfonic acid membranes from liquid water and water vapor. *J. Eelectrochem. Soc.*, 141(6):1493–1498, 1994.

[45] W.Y. Hsu and T.D. Gierke. Ion transport and clustering in Nafion perfluorinated membranes. *J. Membrane Sci.*, 13:307, 1983.

[46] G.S. Hwang and M. Kaviany. Molecular dynamics simulation of effective thermal conductivity of vapor-filled nanogap and nanocavity. *J. Appl. Phys.*, 106:024317–1–6, 2009.

[47] G.S. Hwang, M. Kaviany, J.T. Gostick, A. Weber, and M.H. Kim. Nafion bimodal water wetting and proton/water transport. *J. Phys. Chem. B*, page submitted, 2010.

[48] G.S. Hwang, M. Kaviany, J.H. Nam, M.H. Kim, and S.Y. Son. Pore-water morphological transitions in polymer electrolyte of a fuel cell. *J. Electrochem. Soc.*, 156:B1192–B1200, 2009.

[49] R. Iwamoto, K. Oguro, M. Sato, and Y. Iseki. Water in perfluorinated sulfonic acid Nafion membranes. *J. Phys. Chem. B*, 106:6973–6979, 2002.

[50] P.J. James, M. Antognozzi, J. Tamayo, J. McMaster, J.M. Newton, and M.J. Miles. Interpretation of contrast in tapping mode afm and shear force microscopy. a study of nafion. *Langmuir*, 17:349–360, 2001.

[51] P.J. James, J.A. Elliott, T.J. McMaster, J.M. Newton, A.M.S.Elliott, S. Hanna, and M.J. Miles. Hydration of nafion studied by afm and x-ray scattering. *J. Mat. Sci*, 35:5111–5119, 2000.

[52] J.H. Nam and M. Kaviany. Effective mass diffusivity and water saturation distribution in single- and two-layer PEMFC diffusion medium. *Int. J. Heat Mass Trans.*, 46:4595–4611, 2003.

[53] J.H. Nam, K.J. Lee, G.S. Hwang, C.J. Kim, and M. Kaviany. Microporous layer for water morphology control in PEMFC. *Int. J. Heat Mass Trans.*, 52:2779–2791, 2009.

[54] M. Kaviany. *Principles of Heat Transfer in Porous Media, 2nd Ed.* Srpinger-Verlag, New York, 1999.

[55] Massoud Kaviany. *Heat Transfer Physics.* Cambridge University Press, New York, 2008.

[56] J. Kawamura, K. Hattori, T. Hongo, R. Asayama, N. Kuwata, T. Hattori, and J. Mizusaki. Microscopic states of water and methanol in Nafion membrane observed by NMR micro imaging. *Solid State Ionics*, 176:2451–2456, 2005.

[57] E.H. Kennard. *Kinetic Theory of Gases*. McGraw-Hill, New York, 1938.

[58] N. Kosuke, M. Takeshi, T. Shohji, and H. Shutchiro. Microscopic visualization of state and behavior of liquid water in a gas diffusion layer of PEFC. *Electrochemistry*, 75(2):149–151, 2007.

[59] K.D. Kreuer, S.J. Paddison, E. Spohr, and M. Schuster. Transport in proton conductors for fuel-cell applications: Simulations, elementary reactions, and phenomenology. *Chem. Rev.*, 104:4637–4678, 2004.

[60] I. Kusaka, Z.-G. Wang, and J.H. Seinfeld. Binary nucleation of sulfuric acid-water: Monte carlo simulation. *J. Chem. Phys.*, 108:6829–6848, 1998.

[61] A. Kusoglu, M.H. Santare, and A.M. Karlsson. Mechanics-based model for non-affine swelling in perfluorosulfonic acid (PFSA) membranes. *Polymer*, 50:2481–4291, 2009.

[62] M. Laporta, M. Pegoraro, and L. Zanderighi. Perfluorosulfonated membrane (Nafion): FT-IR study of the state of water with increasing humidity. *Phys. Chem. Chem. Phys.*, 1:4619–4628, 1999.

[63] J. Larminie and A. Dicks. *Fuel Cell Systems Explained*. John Wiley & Sons, Inc., New York, 2000.

[64] G.Q. Lu and X.S. Zhao. *Nanoporous Materials: Science and Engineering (Series on Chemical Engineering)*. Imperial College Press, 2005.

[65] P.W. Majsztrik, A.B. Bocarsly, and J.B. Benziger. Viscoelastic response of nafion. effects of temperature and hydration on tensile creep. *Macromolecules*, 41:9849–9862, 2008.

[66] K. Malek, M. Eikerling, Q. Wang, Z. Liu, S. Otsuka, K. Akizuki, and M. Abe. Nanophase segregation and water dynamics in hydrated Nafion: molecular modeling and experimental validation. *J. Chem. Phys.*, 129:204702–1–10, 2008.

[67] O. Markovitch and N. Agmon. Structure and energetics of the hydronium hydration shells. *J. Phys. Chem. A*, 111:2253–2256, 2007.

[68] D. Marx, M.E. Tuckerman, J. Hutter, and M. Parrinello. The nature of the hydrated excess proton in water. *Nature*, 397:601–604, 1999.

[69] K.A. Mauritz and R.B. Moore. State of understanding of Nafion. *Chem. Rev.*, 104:4535–4585, 2004.

[70] J.P. Meyers. *Simulation and Analysis of the Direct Methanol Fuel Cell*. PhD thesis, University of California-Berkeley, CA, 1998.

[71] C.W. Monroe, T. Romero, W. Mérida, and M. Eikerling. A vaporization-exchange model for water sorption and flux in Nafion. *J. Membr. Sci.*, 324:1–6, 2008.

[72] P. P. Mukherjee, R. Mukundan, J. S. Spendelow, J. R. Davey, R. Borup, D. S. Hussey, D. L. Jacobson, and M. Arif. High resolution neutron imaging of water in the polymer electrolyte fuel cell membrane. *ECS Transactions*, 25(1):505–512, 2009.

[73] D. Nicholson and N.G. Parsonage. *Computer simulation and the statistical mechanics of adsorption*. Academic Press, London, 1982.

[74] R. O'Hayre, S.W. Cha, F.B. Prinz, and W. Colella. *Fuel Cell Fundamentals*. John Wiley & Sons, Inc., New York, 2005.

[75] L.M. Onishi, J.M. Prausnitz, and J. Newman. Water-Nafion equilibria. absence of schroeder's paradox. *J. Phys. Chem. B*, 111:10166–10173, 2007.

[76] S.J. Paddison and J.A. Elliott. Molecular flexibility in the short-side-chain perfluorosulfonic acid membrane. *ECS Transactions*, 1:207–214, 2006.

[77] S.J. Paddison and J.A. Elliott. On the consequences of side chain flexibility and backbone conformation on hydration and proton dissociation in perfluorosulfonic acid membranes. *Phys. Chem. Chem. Phys.*, 8:2193–2203, 2006.

[78] U. Pasaogullari and C.Y. Wang. Liquid water transport in gas diffusion layer of polymer electrolyte fuel cells. *J. Eelectrochem. Soc.*, 151(2):A399–A406, 2004.

[79] J. Puibasset and R. Pellenq. Water adsorption in disordered mesoporous silica (vycor) at 300 k and 650 k: A grand canonical monte carlo simulation study of hysteresis. *J. Chem. Phys.*, 122:094704–1–10, 2005.

[80] R.A. Robinson and R.H. Stokes. *Electrolyte Solutions, 2nd Ed.* Dover Publications, New York, 2002.

[81] J.-P. Ryckaert, G. Ciccotti, and H.J.C. Berendsen. Numerical integration of the cartesian equations of motion of a system with constraints: molecular dynamics of n-alkanes. *J. Comput. Phys.*, 23:327–341, 1977.

[82] W.F. Saam and M.W. Cole. Excitation and thermodynamics for liquid-helium films. *Physics Review B*, 11:1086–1105, 1975.

[83] K. Schmidt-Rohr and Q. Chen. Parallel cylindrical water nanochannels in Nafion fuel-cell membranes. *Nature Mat.*, 7:75–83, 2008.

[84] S.K. Singh, A. Sinha, G. Deo, and J.K. Singh. Vapor-liquid phase coexistence, critical properties, and surface tension of confined alkanes. *J. Phys. Chem. C*, 113:7170–7180, 2009.

[85] Y. Sone, P. Ekdunge, and D. Simonsson. Proton conductivity of Nafion 117 as measured by a four-electrode AC impedance method. *J. Electrochem. Soc.*, 143(4):1254–1259, 1996.

[86] D. Spernjak, P. Mukherjee, R. Mukundan, J. Davey, D. Hussey, D. Jacobson, and R. Borup. Measurement of water content in polymer electrolyte membranes using high resolution neutron imaging. Las Vegas, CA, 2010. 218^{th} ECS Meeting.

[87] E. Sphor. Molecular dynamics simulations of proton transfer in a model Nafion pore. *Molecular Simulation*, 30:107–115, 2004.

[88] T.E. Springer, T.A. Zawodzinski, and S. Gottesfeld. Polymer electrolyte fuel cell model. *J. Eelectrochem. Soc.*, 138(8):2334–2342, 1991.

[89] E. Stöckelmann, E.M. Aydt, and R. Hentschke. Simulation of adsorption isotherms of water on ionic surfaces. *J. Mol. Model.*, 3:347–354, 1997.

[90] M.-L. Tan, J.T. Fischer, A. Chandra, B.R. Brooks, and T. Ichiye. A temperature of maximum density in soft sticky dipole water. *Chem. Phys. Lett.*, 376:646–652, 2003.

[91] M.E. Tuckerman, D. Marx, and M. Parrinello. The nature and transport mechanism of hydrated hydroxide ions in aqueous solution. *Nature*, 417:925–929, 2002.

[92] A. Weber and J. Newman. Coupled thermal and water management in polymer electrolyte fuel cells. *J. Eelectrochem. Soc.*, 153(12):A2205–A2214, 2006.

[93] A.Z. Weber and M.A. Hickner. Modeling and high-resolution-imaging studies of water-content profiles in a polymer-electrolyte-fuel-cell membrane-electrode assembly. *Electrochim. Acta*, 53(26):7668–7674, 2008.

[94] A.Z. Weber and J. Newman. Transport in polymer-electrolyte membranes, I. Physical model. *J. Eelectrochem. Soc.*, 150(7):A1008–A1015, 2003.

[95] A.Z. Weber and J. Newman. Transport in polymer-electrolyte membranes, III. Model validation in a simple fuel-cell model. *J. Eelectrochem. Soc.*, 151(2):A326–A339, 2004.

[96] A.Z. Weber and J. Newman. Effects of microporous layers in polymer electrolyte fuel cells. *J. Eelectrochem. Soc.*, 152(4):A677–A688, 2005.

[97] J.T. Wescott, Y. Qi, L. Subramanian, and T.W. Carpehart. Mesoscale simulation of morphology in hydrated perfulorosulfonic acid membranes. *J. Chem. Phys.*, 124:134702–1–14, 2006.

[98] X. Ye and C.Y. Wang. Measurement of water transport properties through membrane-electrode assemblies, I. Membranes. *J. Eelectrochem. Soc.*, 154(7):B676–B682, 2007.

[99] H.L. Yeager and A. Steck. Cation and water diffusion in nation ion exchange membranes: Influence of polymer structure. *J. Eelectrochem. Soc.*, 128(9):1880–1884, 1981.

[100] G. J. Zarragoicoechea and V.A. Kuz. Critical shift of a confined fluid in a nanopore. *Fluid Phase Equilibr*, 220:7–9, 2004.

[101] T.A. Zawodzinski, C. Derouin, S. Radzinski, R.J. Sherman, V.T. Smith, T.E. Springer, and S. Gottesfeld. Water uptake by and transport through Nafion 117 membranes. *J. Eelectrochem. Soc.*, 140(4):1041–1047, 1993.

[102] T.A. Zawodzinski, Jr., M. Neeman, L.O. Sillerud, and S. Gottesfeld. Determination of water diffusion coefficients in perfluorosulfonate ionomeric membranes. *J. Phys. Chem.*, 95:6040–6044, 1991.

[103] T.A. Zawodzinski, S. Gottesfeld Jr., S. Shoichet, and T.J. McCarthy. Contact angle between water and the surface of perfluorosulphonic acid membranes. *J. Appl. Elecrochem.*, 23:86–88, 1993.

[104] T.A. Zawodzinski, T.E. Springer, J. Davey, R.Jestel, C. Lopez, J. Valerio, and S. Gottesfeld. A comparative study of water uptake by and transport through ionomeric fuel cell membranes. *J. Eelectrochem. Soc.*, 140(7):1981–1985, 1993.

[105] X. Zhou, Z. Chen, F. Delgado, D. Brenner, and R. Srivastava. Atomistic simulation of conduction and diffusion processes in Nafion polymer electrolyte and experimental validation. *J. Electrochem. Soc.*, 154:B82–B87, 2007.

[106] G. Zundel. Hydration structure and intermolecular interaction in polyelectrolytes. *Angew. Chem. Int. Edit.*, 8(7):499–509, 1969.